Inorganic Chemistry
Article

Inorg. Chem. **2011**, *50*, 155–171 **155**
DOI: 10.1021/ic101535y

Molecular and Electronic Structures of Dinuclear Iron Complexes Incorporating Strongly Electron-Donating Ligands: Implications for the Generation of the One- and Two-Electron Oxidized Forms

Julia B. H. Strautmann,[†] Carl-Georg Freiherr von Richthofen,[†] Gabriele Heinze-Brückner,[†] Serena DeBeer,[‡] Eberhard Bothe,[§] Eckhard Bill,[§] Thomas Weyhermüller,[§] Anja Stammler,[†] Hartmut Bögge,[†] and Thorsten Glaser*[,†]

[†]*Fakultät für Chemie, Universität Bielefeld, Universitätsstrasse 25, D-33615 Bielefeld, Germany,* [‡]*Cornell University, Department of Chemistry and Chemical Biology, Ithaca, New York 14853, United States, and* [§]*Max-Planck-Institut für Bioanorganische Chemie, Stiftsstrasse 34-36, D-45470 Mülheim, Germany*

Received July 30, 2010

The ligands $(L^{t\text{-}Bu_2})^{2-}$, $(L^{Me_2})^{2-}$, and $(L^{Cl_2})^{2-}$ have been employed for the synthesis of the dinuclear Fe^{III} complexes $[L^{t\text{-}Bu_2}Fe(\mu\text{-}O)FeL^{t\text{-}Bu_2}]$, $[L^{Me_2}Fe(\mu\text{-}O)FeL^{Me_2}]$, and $[L^{Cl_2}Fe(\mu\text{-}O)FeL^{Cl_2}]$. The strongly electron-donating groups (*tert*-amines and phenolates) were chosen to increase the electron density at the coordinated ferric ions and thus to facilitate the oxidation of the complexes, with the possibility of fine-tuning the electronic structures by variation of the remote substituents. Molecular structures established in the solid (by single-crystal X-ray diffraction) and in solution (by X-ray absorption spectroscopy) show that the Fe ions are five-coordinate in a square-pyramidal coordination environment with the ligand adopting a *trans*-conformation. Spectroscopic and magnetic characterization establishes the highly covalent nature of the $Fe^{III}-O^{oxo}$ and $Fe^{III}-O^{Ph}$ bonds. The variations in the donor capabilities of the phenolates (due to changes in the remote substituents) are compensated for by a flexible electron donation of the $Fe^{III}-O^{oxo}$ bonding. Spectroelectrochemical characterization demonstrates that $[L^{t\text{-}Bu_2}Fe(\mu\text{-}O)FeL^{t\text{-}Bu_2}]$ can be oxidized reversibly at +0.27 and +0.44 V versus Fc^+/Fc, whereas $[L^{Me_2}Fe(\mu\text{-}O)FeL^{Me_2}]$ and $[L^{Cl_2}Fe(\mu\text{-}O)FeL^{Cl_2}]$ exhibit irreversible oxidations at +0.29 and +0.87 V versus Fc^+/Fc, respectively. UV−vis, electron paramagnetic resonance (EPR), X-ray absorption spectroscopy (XAS), and Mössbauer spectroscopy show that the successive oxidations of $[L^{t\text{-}Bu_2}Fe(\mu\text{-}O)FeL^{t\text{-}Bu_2}]$ are ligand-centered leading to the monophenoxyl radical complex $[^{\bullet}L^{t\text{-}Bu_2}Fe^{III}\text{-}(\mu\text{-}O)Fe^{III}L^{t\text{-}Bu_2}]^+$ (with the oxidation primarily localized on one-half of the molecule) and the diphenoxyl radical complex $[^{\bullet}L^{t\text{-}Bu_2}Fe^{III}(\mu\text{-}O)Fe^{III\bullet}L^{t\text{-}Bu_2}]^{2+}$. Both products are unstable in solution and decay by cleavage of an $Fe^{III}-O^{oxo}$ bond. The two-electron oxidized species is more stable because of two equally strong $Fe^{III}-O^{oxo}$ bonds, whereas in the singly oxidized species the $Fe^{III}-O^{oxo}$ bond of the non-oxidized half is weakened. The decay of the monocation results in the formation of $[L^{t\text{-}Bu_2}Fe^{III}]^+$ and $[L^{t\text{-}Bu_2}Fe^{IV}{=}O]$, while the decay of the dication yields $[^{\bullet}L^{t\text{-}Bu_2}Fe^{III}]^{2+}$ and $[L^{t\text{-}Bu_2}Fe^{IV}{=}O]$. Follow-up reactions of the oxidized fragments with the counteranion of the oxidant, $[SbCl_6]^-$, leads to the formation of $[Fe^{III}Cl_4]^-$.

1. Introduction

Methane monooxygenase (MMO),[1,2] stearyl ACP Δ^9-desaturase (Δ9D),[3] and ribonucleotide reductase (RNR)[4,5] belong to a class of metalloenzymes that activate dioxygen at nonheme diiron active sites to carry out diverse oxidations/hydroxylations. The mechanisms for dioxygen activation appear to involve high-valent species.[6−15] The active species

*To whom correspondence should be addressed. E-mail: thorsten.glaser@uni-bielefeld.de.

(1) Rosenzweig, A. C.; Frederick, C. A.; Lippard, S. J.; Nordlund, P. *Nature* **1993**, *366*, 537–543.
(2) Rosenzweig, A. C.; Nordlund, P.; Takahara, P. M.; Frederick, C. A.; Lippard, S. J. *Chem. Biol.* **1995**, *2*, 409–418.
(3) Lindqvist, Y.; Huang, W.; Schneider, G.; Shanklin, J. *EMBO J.* **1996**, *15*, 4081–4092.
(4) Nordlund, P.; Sjöberg, B.-M.; Eklund, H. *Nature* **1990**, *345*, 393–398.
(5) Logan, D. T.; Su, X.-D.; Aberg, A.; Regnstrom, K.; Hadju, J.; Eklund, H.; Nordlund, P. *Structure* **1996**, *4*, 1053–1064.
(6) Lee, S.-K.; Nesheim, J. C.; Lipscomb, J. D. *J. Biol. Chem.* **1993**, *268*, 21569–21577.
(7) Lee, S.-K.; Fox, B. G.; Froland, W. A.; Lipscomb, J. D.; Münck, E. *J. Am .Chem. Soc.* **1993**, *115*, 6450–6451.
(8) Liu, K. E.; Valentine, A. M.; Wang, D.; Huynh, B. H.; Edmondson, D. E.; Salifoglou, A.; Lippard, J. *J. Am .Chem. Soc.* **1995**, *117*, 10174–10185.
(9) Shu, L.; Nesheim, J. C.; Kauffmann, K.; Münck, E.; Lipscomb, J. D.; Que, L., Jr. *Science* **1997**, *275*, 515–518.
(10) Waller, B. J.; Lipscomb, J. D. *Chem. Rev.* **1996**, *96*, 2625–2657.
(11) Solomon, E. I.; Brunold, T. C.; Davis, M. I.; Kemsley, J. N.; Lee, S.-K.; Lehnert, N.; Neese, F.; Skulan, A. J.; Yang, Y.-S.; Zhou, J. *Chem. Rev.* **2000**, *100*, 235–349.
(12) Feig, A. L.; Lippard, S. *J. Chem. Rev.* **1994**, *94*, 759–805.

Published on Web 11/29/2010

Scheme 1

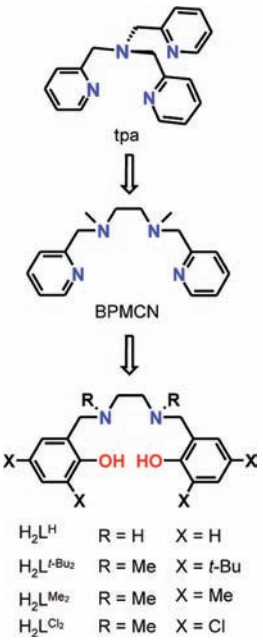

in MMO, compound **Q**, is proposed to consist of a high-valent $Fe^{IV}(\mu\text{-}O)_2Fe^{IV}$ core, which hydroxylates methane to methanol. A similar oxo-bridged $Fe^{III}Fe^{IV}$ species, intermediate **X**, is found in the catalytic cycle of RNR,[13] which was first designated a $Fe^{III}Fe^{III}$ radical species by Mössbauer and electron paramagnetic resonance (EPR) spectra (isotropic EPR signal at $g = 2.00$).[16]

There have been significant efforts to characterize dinuclear high-valent complexes that may serve as models for the oxidizing intermediates in oxygen activating enzymes.[17−26] Using ring-alkylated derivatives of the ligand tpa (Scheme 1), Que and co-workers have synthesized $Fe^{III}(\mu\text{-}O)_2Fe^{IV}$ complexes[22,23] that are capable of oxidizing hydrocarbons and phenols.[27] Later, they used linear tetradentate ligands, such as BPMCN (Scheme 1),[28,29] in which a pyridine donor has been replaced by a *tert*-amine donor and the ligand topology is altered. In comparison to tertiary amines, pyridine is a weaker σ-donor ligand with some π-acceptor capabilities, and thus reduces the electron density of the metal atom to which it is coordinated.

To stabilize high-valent dinuclear iron complexes, our strategy is to increase the electron density at the iron atoms by using a ligand system with a set of strongly electron-donating ligands. This may be achieved by the substitution of the two remaining pyridine donors in BPMCN by two phenolato donors (Scheme 1). Phenolato donors are not only strong σ-donor ligands but also strong π-donor ligands and they form highly covalent bonds with transition metal ions.[30] In this respect, it is interesting to note that during the course of our studies, Que et al. succeeded in the electrochemical generation and characterization of an $Fe^{IV}(\mu\text{-}O)_2Fe^{IV}$ complex,[31] stabilized by a tpa ligand derivative with two methyl and one methoxy substituent on each pyridine ring. Consistent with our strategy, these electron-donating substituents increase the electron density at the iron atom facilitating its oxidation to Fe^{IV}.

The use of a variety of substituted *N*,*N*′-bis(2-hydroxybenzyl)-1,2-diaminoethane ligands (Scheme 1) for the synthesis of dinuclear iron complexes has been described previously.[32−34] Using the unsubstituted parent ligand *N*,*N*′-bis(2-hydroxybenzyl)-1,2-diaminoethane (H_2L^H) the dinuclear complexes $[L^HFe^{III}(\mu\text{-}OH)_2Fe^{III}L^H]$ with two bridging hydroxo groups[32] and $[L^HFe^{III}(\mu\text{-}OMe)_2Fe^{III}L^H]$ with two bridging methoxo groups[33] were synthesized. A bis-methoxo brigded complex was also reported using the 3-methyl-5-*tert*-butylphenol derivative of H_2L^H.[34] It should be noted that no oxidative chemistry was reported.

We have chosen the *tert*-amine *N*,*N*′-dimethyl-1,2-diaminoethane backbone to further stabilize potential high-valent iron complexes and to protect the ligand from degradation. *Tert*-amines have been shown to stabilize high-valent Fe^{IV}=O complexes,[35] although the origin of this stabilization is still controversial.[36−38] In addition, the ligand $H_2L^{t\text{-}Bu_2}$ possesses *t*-butyl groups in *ortho*- and *para*-position to the phenol which allows for (*i*) increased electron density at the phenolates (because of the electron donating nature of the *tert*-butyl groups) and (*ii*) protection of the ligand from degradation processes (as the *ortho*- and *para*-positions

(13) Sturgeon, B. E.; Burdi, D.; Chen, S.; Huynh, B.-H.; Edmondson, D. E.; Stubbe, J.; Hoffman, B. M. *J. Am. Chem. Soc.* **1996**, *118*, 7551–7557.
(14) Merkx, M.; Kopp, D. A.; Sazinsky, M. H.; Blazyk, J. L.; Müller, J.; Lippard, S. L. *Angew. Chem., Int. Ed.* **2001**, *40*, 2782–2807.
(15) Lee, D.; Lippard, J. In *Comprehensive Coordination Chemistry*; McCleverty, J. A., Meyer, T. J., Eds.; Elsevier Ltd.: Oxford, 2004; Vol. *II*, pp 309−342.
(16) Ravi, N.; Bollinger, J. M., Jr.; Huynh, B. H.; Edmondson, D. E.; Stubbe, J. *J. Am. Chem. Soc.* **1994**, *116*, 8007–8014.
(17) Lee, D.; Du Bois, J.; Petasis, D.; Hendrich, M. P.; Krebs, C.; Huynh, B. H.; Lippard, S. J. *J. Am. Chem. Soc.* **1999**, *121*, 9893–9894.
(18) Que, L., Jr.; Tolman, W. B. *Angew. Chem.* **2002**, *114*, 1160–1185.
(19) Que, L., Jr. *J. Chem. Soc., Dalton Trans.* **1997**, 3933–3940.
(20) Que, L., Jr.; Dong, Y. *Acc. Chem. Res.* **1996**, *29*, 190–196.
(21) Tshuva, E. Y.; Lippard, S. *J. Chem. Rev.* **2004**, *104*, 987–1012.
(22) Dong, Y.; Fujii, H.; Hendrich, M. P.; Leising, R. A.; Pan, G.; Randall, C. R.; Wilkinson, E. C.; Zang, Y.; Que, L., Jr.; Fox, B. G.; Kauffmann, K.; Münck, E. *J. Am. Chem. Soc.* **1995**, *117*, 2778–2792.
(23) Hsu, H.-F.; Dong, Y.; Shu, L.; Young, V. G. J.; Que, L., Jr. *J. Am. Chem. Soc.* **1999**, *121*, 5230–5237.
(24) Ghosh, A.; De Oliveira, F. T.; Yano, T.; Nishioka, T.; Beach, E. S.; Kinoshita, I.; Münck, E.; Ryabov, A. D.; Horwitz, C. P.; Collins, T. J. *J. Am . Chem. Soc.* **2005**, *127*, 2505–2513.
(25) Wang, D.; Farquhar, E. R.; Stubna, A.; Münck, E.; Que, L., Jr. *Nat. Chem.* **2009**, *1*, 145–150.
(26) Xue, G.; De Hont, R.; Münck, E.; Que, L. *Nat. Chem.* **2010**, *2*, 400–405.
(27) Kim, C.; Dong, Y.; Que, L., Jr. *J. Am. Chem. Soc.* **1997**, *119*, 3635–3636.
(28) Costas, M.; Rohde, J.-U.; Stubna, A.; Ho, R. Y. N.; Quaroni, H.; Münck, E.; Que, L., Jr. *J. Am. Chem. Soc.* **2001**, *123*, 12931–12932.
(29) Jensen, M. P.; Costas, M.; Ho, R. Y. N.; Kaizer, J.; Mairata i Payeras, A.; Münck, E.; Que, L., Jr.; Rohde, J.-U.; Stubna, A. *J. Am. Chem. Soc.* **2005**, *127*, 10512–10525.
(30) Izumi, Y.; Glaser, T.; Rose, K.; McMaster, J.; Basu, P.; Enemark, J. H.; Hedman, B.; Hodgson, K. O.; Solomon, E. I. *J. Am. Chem. Soc.* **1999**, *121*, 10035–10046.
(31) Xue, G.; Wang, D.; De Hont, R.; Fiedler, A. T.; Shan, X.; Münck, E.; Que, L., Jr. *Proc. Natl. Acad. Sci. U.S.A.* **2007**, *104*, 20713–20718.
(32) Borer, L.; Thalken, L.; Ceccarelli, C.; Glick, M.; Zhang, J. H.; Reiff, W. M. *Inorg. Chem.* **1983**, *22*, 1719–1724.
(33) Viswanathan, R.; Palaniandavar, M.; Prabakaran, P.; Muthiah, P. T. *Inorg. Chem.* **1988**, *37*, 3881–3884.
(34) Baran, P.; Böttcher, A.; Elias, H.; Haase, W.; Hüber, M.; Fuess, H.; Paulus, H. *Z. Naturforsch. B* **1992**, *47*, 1681–1686.
(35) Rohde, J.-U.; In, J.-H.; Lim, M. H.; Brennessel, W. W.; Bukowski, M. R.; Stubna, A.; Münck, E.; Nam, W.; Que, L., Jr. *Science* **2003**, *299*, 1037–1039.
(36) Meyerstein, D. *Coord. Chem. Rev.* **1999**, *185*−*186*, 141–147.
(37) Bessac, F.; Frenking, G. *Inorg. Chem.* **2006**, *45*, 6956–6964.
(38) Berry, J. F.; Bill, E.; Garcia-Serres, R.; Neese, F.; Weyhermüller, T.; Wieghardt, K. *Inorg. Chem.* **2006**, *45*, 2027–2037.

may possess partial radical character once coordinated to a metal ion).[39,40]

We have prepared and fully characterized the mononuclear complexes [$L^{t\text{-}Bu_2}$FeCl] and [$L^{t\text{-}Bu_2}$Fe(η^2-NO_3)] in the solid-state as well as in solution.[41] Electrochemical analysis established two reversible oxidation waves for [$L^{t\text{-}Bu_2}$FeCl] at +0.55 V and +0.93 V versus Fc^+/Fc and one reversible oxidation wave at +0.59 V with an irreversible oxidation at +1.07 V versus Fc^+/Fc for [$L^{t\text{-}Bu_2}$Fe(η^2-NO_3)]. Spectroelectrochemical studies provide the formulation for [$L^{t\text{-}Bu_2}$FeCl]$^+$ as an Fe^{III} monophenoxyl radical complex and for [$L^{t\text{-}Bu_2}$FeCl]$^{2+}$ as an Fe^{III} diphenoxyl radical complex.

The dinuclear complex [$L^{t\text{-}Bu_2}Fe^{III}$($\mu$-O)$Fe^{III}L^{t\text{-}Bu_2}$] exhibits low potentials for the reversible one- and two-electron oxidation at 0.27 and 0.44 V versus Fc^+/Fc, respectively.[42] Recently, we communicated the electrochemical and chemical generation of [$L^{t\text{-}Bu_2}$Fe(μ-O)Fe$L^{t\text{-}Bu_2}$]$^+$ and [$L^{t\text{-}Bu_2}$Fe(μ-O)Fe$L^{t\text{-}Bu_2}$]$^{2+}$.[43] Spectroscopic characterization proved the monocation to be best described as a monophenoxyl radical complex [$^{\bullet}L^{t\text{-}Bu_2}Fe^{III}$($\mu$-O)$Fe^{III}L^{t\text{-}Bu_2}$]$^+$ and the dication as a diphenoxyl radical complex [$^{\bullet}L^{t\text{-}Bu_2}Fe^{III}$($\mu$-O)$Fe^{III\bullet}L^{t\text{-}Bu_2}$]$^{2+}$. Time-dependent spectroscopic tracking showed that both oxidized complexes decay by forming mononuclear complexes.[43]

These studies revealed two inherent properties of the ligand $H_2L^{t\text{-}Bu_2}$: (*i*) this ligand does not form bis-μ-hydroxo-bridged Fe^{III} complexes as the derivatives of the ligand H_2L^H do, and (*ii*) the oxidation of the dinuclear complex is ligand-centered leading to coordinated phenoxyl radicals and not metal-centered leading to Fe^{IV} complexes. Both properties might be attributed to the strong electron donation of the $H_2L^{t\text{-}Bu_2}$ ligand. The increased electron density at the iron leads to a preference for a 5-coordinate μ-oxo-bridged species instead of 6-coordinate bis-μ-hydroxo-bridged species (as realized by the use of the ligand H_2L^H). In addition, the electron density in the phenolate rings results in a highest occupied molecular orbital (HOMO) with significant phenolate character and thus a ligand-centered oxidation. To reduce the electron density in the phenolate-rings and thus the electron-donating character of the ligand, we substituted the remote *t*-butyl groups by less donating methyl groups ($H_2L^{Me_2}$) or alternatively by chloro substituents ($H_2L^{Cl_2}$). Herein, we provide a study on the three complexes [$L^{t\text{-}Bu_2}$Fe(μ-O)Fe$L^{t\text{-}Bu_2}$],[42,43] [L^{Me_2}Fe(μ-O)FeL^{Me_2}], and [L^{Cl_2}Fe(μ-O)FeL^{Cl_2}]. The detailed comparison of their properties provides insight into the electronic properties of the Fe^{III}(μ-O)Fe^{III} core by variation of remote phenolate substituents. Additionally, we investigate the decay products of [$^{\bullet}L^{t\text{-}Bu_2}Fe^{III}$($\mu$-O)$Fe^{III}L^{t\text{-}Bu_2}$]$^+$ and [$^{\bullet}L^{t\text{-}Bu_2}$-$Fe^{III}$($\mu$-O)$Fe^{III\bullet}L^{t\text{-}Bu_2}$]$^{2+}$.

2. Experimental Section

Solvents and starting materials were of the highest commercially available purity and were used as received except were noted. CH_2Cl_2 used for the chemical oxidations, was dried over CaH_2 and distilled under an argon atmosphere before use. The syntheses of $H_2L^{t\text{-}Bu_2}$,[44−46] $H_2L^{Me_2}$,[44,47] $H_2L^{Cl_2}$,[45,48] and [$L^{t\text{-}Bu_2}$Fe(μ-O)Fe$L^{t\text{-}Bu_2}$][42] have been described previously.

[L^{Me_2}Fe(μ-O)FeL^{Me_2}]. A solution of $Fe(ClO_4)_3\cdot 10H_2O$ (107 mg, 0.20 mmol) in ethanol (5 mL) was added to a suspension of the ligand $H_2L^{Me_2}$ (71 mg, 0.20 mmol) in ethanol (5 mL). A blue solution was obtained, to which a solution of triethylamine (81 mg, 0.80 mmol) in ethanol (2 mL) was added dropwise. The dark blue solution was heated to reflux for 2 h and filtered after cooling. By slow evaporation of the solvent, dark red crystals of [L^{Me_2}Fe(μ-O)FeL^{Me_2}] suitable for single-crystal X-ray diffraction formed within a few weeks. Yield: 139 mg (83%). MS-MALDI-TOF: m/z = 837 (46) $[M + H]^+$, 426 (24) [$L^{Me_2}Fe{=}O]^+$, 410 (100) [$L^{Me}Fe]^+$. IR (KBr): $\tilde{\nu}/cm^{-1}$ = 2989 w, 2964 w, 2908 m, 2857 m, 1611 w, 1475 s, 1419 m, 1366 w, 1315 s, 1271 s, 1161 m, 862 s, 817 s, 795 m, 540 m, 507 w. Anal. Calcd for [L^{Me_2}Fe(μ-O)-FeL^{Me_2}]$\cdot H_2O$, $C_{44}H_{62}N_4O_6Fe_2$, 854.68 g/mol: C 61.83, H 7.31, N 6.56. Found: C 61.64, H 7.32, N 6.57.

[L^{Cl_2}Fe(μ-O)FeL^{Cl_2}]. A solution of the ligand $H_2L^{Cl_2}$ (964 mg, 2.200 mmol) in CH_2Cl_2 (60 mL) and a solution of triethylamine (890 mg, 8.80 mmol) in ethanol (20 mL) were added dropwise to a solution of $Fe(ClO_4)_3\cdot 10H_2O$ (1.176 g, 2.201 mmol) in ethanol (60 mL). The purple solution was heated to reflux for 2 h. After cooling, the orange precipitate of [L^{Cl_2}Fe(μ-O)FeL^{Cl_2}] was filtered off. Slow evaporation of the filtrate yielded orange crystals of [L^{Cl_2}Fe(μ-O)FeL^{Cl_2}] suitable for single-crystal X-ray diffraction. Orange crystals of [L^{Cl_2}Fe(μ-O)FeL^{Cl_2}]$\cdot CH_2Cl_2$ suitable for single-crystal X-ray diffraction were obtained by slow evaporation of a solution of the precipitate in CH_2Cl_2/ethanol (3:2). Yield: 1.035 g (92%). MS-MALDI-TOF: m/z = 508 (64) [$L^{Cl_2}Fe{=}O]^+$, 492 (100) [$L^{Cl_2}Fe]^+$. IR (KBr): $\tilde{\nu}/cm^{-1}$ = 3078 w, 3015 w, 2982 w, 2914 w, 2885 w, 2812 w, 1583 w, 1456 s, 1423 m, 1371 w, 1315 s, 1286 m, 1250 w, 1221 m, 1178 m, 866 m, 853 m, 829 m, 760 s. Anal. Calcd for [L^{Cl_2}Fe(μ-O)FeL^{Cl_2}], $C_{36}H_{36}N_4O_5Cl_8Fe_2$, 1000.01 g/mol: C 43.24, H 3.63, N 5.60. Found: C 43.30, H 3.71, N 5.59.

The detailed procedures for the preparation of the oxidized species and the experimental details for the physical methods are provided in the Supporting Information.

3. Results and Analysis

3.1. Synthesis and Characterization. The reactions of the ligand $H_2L^{t\text{-}Bu_2}$ with Fe^{III} salts and 2 equiv of a base results in the deposition of blue crystals. Starting from $FeCl_3$ the mononuclear complex [$L^{t\text{-}Bu_2}$FeCl] formed while starting from $FeNO_3\cdot 9H_2O$ yields the mononuclear complex [$L^{t\text{-}Bu_2}$Fe(η^2-NO_3)].[41] Using 3 equiv of a base, the reaction solution turned from blue to red, and red crystals of [$L^{t\text{-}Bu_2}$Fe(μ-O)Fe$L^{t\text{-}Bu_2}$] formed.[42] In the case of the ligands $H_2L^{Me_2}$ and $H_2L^{Cl_2}$ 4 equiv of a base have been necessary to obtain the μ-oxo-bridged complexes [L^{Me_2}Fe(μ-O)FeL^{Me_2}] and [L^{Cl_2}Fe(μ-O)FeL^{Cl_2}], respectively.

(39) Adam, B.; Bill, E.; Bothe, E.; Goerdt, B.; Haselhorst, G.; Hildenbrand, K.; Sokolowski, A.; Steenken, S.; Weyhermüller, T.; Wieghardt, K. *Chem.—Eur. J.* **1997**, *3*, 308–319.

(40) Sokolowski, A.; Muller, J.; Weyhermuller, T.; Schnepf, R.; Hildebrandt, P.; Hildenbrand, K.; Bothe, E.; Wieghardt, K. *J. Am. Chem. Soc.* **1997**, *119*, 8889–8900.

(41) Strautmann, J. B. H.; DeBeer George, S.; Bothe, E.; Bill, E.; Weyhermüller, T.; Stammler, A.; Bögge, H.; Glaser, T. *Inorg. Chem.* **2008**, *47*, 6804–6824.

(42) Glaser, T.; Pawelke, R. H.; Heidemeier, M. *Z. Anorg. Allg. Chem.* **2003**, *629*, 2274–2281.

(43) Strautmann, J. B. H.; Frhr. v. Richthofen, C.-G.; DeBeer George, S.; Bothe, E.; Bill, E.; Glaser, T. *Chem. Commun.* **2009**, 2637–2639.

(44) Tshuva, E. Y.; Goldberg, I.; Kol, M. *J. Am. Chem. Soc.* **2000**, *122*, 10706–10707.

(45) Hormnirum, P.; Marshall, E. L.; Gibson, V. C.; White, A.; Williams, D. J. *J. Am. Chem. Soc.* **2004**, *126*, 2688–2689.

(46) Balsells, J.; Carroll, P. J.; Walsh, T. J. *Inorg. Chem.* **2001**, *40*, 5568–5574.

(47) Tshuva, E. Y.; Gendeziuk, N.; Kol, M. *Tetrahedron Lett.* **2001**, *42*, 6405–6407.

(48) Segal, S.; Goldberg, I.; Kol, M. *Organometallics* **2005**, *24*, 200–202.

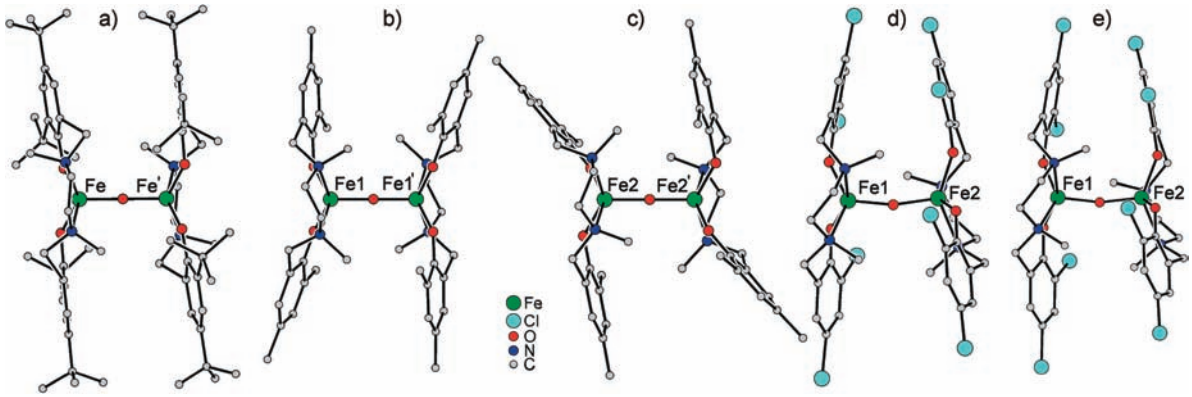

Figure 1. Molecular structures of (a) $[L^{t\text{-}Bu_2}Fe(\mu\text{-}O)FeL^{t\text{-}Bu_2}]$,[42] (b) $[L^{Me_2}Fe(\mu\text{-}O)FeL^{Me_2}]$ (molecule 1), (c) $[L^{Me_2}Fe(\mu\text{-}O)FeL^{Me_2}]$ (molecule 2), (d) $[L^{Cl_2}Fe(\mu\text{-}O)FeL^{Cl_2}]$, and (e) $[L^{Cl_2}Fe(\mu\text{-}O)FeL^{Cl_2}]$ in $[L^{Cl_2}Fe(\mu\text{-}O)FeL^{Cl_2}]\cdot CH_2Cl_2$.

Table 1. Selected Structural Parameters Obtained from Single-Crystal X-ray Diffraction[a]

	d(Fe−O^{oxo})/Å	d(Fe−O^{Ph})/Å	d(Fe−N)/Å	d_{av}(C−C)$_{ar}$/Å	d(C−O^{Ph})/Å	∠(Fe−O−Fe)/deg	τ
$[L^{t\text{-}Bu_2}Fe(\mu\text{-}O)FeL^{t\text{-}Bu_2}]$[42]	1.782(1)	1.852(5)	2.210(5)	1.38	1.344(10)	180	0.17
		1.865(5)	2.244(5)		1.350(10)		
$[L^{Me_2}Fe(\mu\text{-}O)FeL^{Me_2}]$ (mol. 1)	1.784(1)	1.912(2)	2.238(2)	1.40	1.342(3)	180	0.04
		1.897(2)	2.233(2)		1.340(3)		
$[L^{Me_2}Fe(\mu\text{-}O)FeL^{Me_2}]$ (mol. 2)	1.781(1)	1.906(2)	2.259(2)	1.40	1.331(3)	180	0.20
		1.902(2)	2.203(2)		1.338(3)		
$[L^{Cl_2}Fe(\mu\text{-}O)FeL^{Cl_2}]$	1.772(1)	1.915(1)	2.208(2)	1.39	1.318(2)	166.12(10)	0.32
	1.772(1)	1.903(1)	2.258(2)		1.320(2)		0.26
		1.927(1)	2.207(2)		1.317(3)		
		1.904(1)	2.273(2)		1.324(3)		
$[L^{Cl_2}Fe(\mu\text{-}O)FeL^{Cl_2}]\cdot CH_2Cl_2$	1.771(2)	1.902(3)	2.287(3)	1.39	1.317(4)	166.32(18)	0.32
	1.774(2)	1.927(3)	2.187(3)		1.322(4)		0.35
		1.905(3)	2.265(3)		1.334(4)		
		1.927(3)	2.205(3)		1.320(4)		
$H_2L^{Me_2}$				1.39	1.370(1)		
$H_2L^{Cl_2}$				1.39	1.349(2)		

[a] For detailed listings including atom numbering see Tables S1−S5 in the Supporting Information.

All three complexes $[L^{X_2}Fe(\mu\text{-}O)FeL^{X_2}]$ are soluble in common organic solvents. However, only solutions in non-protic and non-coordinating solvents like CH_2Cl_2 or toluene exhibit a red to orange color, as observed for all three complexes in the solid state. Dissolution of the complexes in alcoholic solvents, acetonitrile, acetone, or even tetrahydrofuran (THF) results in the formation of deep blue solutions indicating the formation of mononuclear complexes and therefore an $Fe^{III}-O^{oxo}$ bond cleavage. The instability of the dinuclear complexes is corroborated by mass spectrometric analysis. Matrix-assisted laser desorption/ionization-time of flight (MALDI-TOF) mass spectra of $[L^{t\text{-}Bu_2}Fe(\mu\text{-}O)FeL^{t\text{-}Bu_2}]$ and $[L^{Cl_2}Fe(\mu\text{-}O)FeL^{Cl_2}]$ do not exhibit a signal corresponding to a $[M]^+$ or $[M+H]^+$ ion, whereas the spectra of $[L^{Me_2}Fe(\mu\text{-}O)FeL^{Me_2}]$ exhibit a prominent signal corresponding to the $[M+H]^+$ ion. All three spectra feature signals corresponding to the ions $[L^{X_2}Fe{=}O]^+$ and $[L^{X_2}Fe]^+$. In all three cases, the $[L^{X_2}Fe]^+$ signal is the most intense signal followed by the $[L^{X_2}Fe{=}O]^+$ signal. These data are consistent with cleavage of an $Fe^{III}-O^{oxo}$ bond under MALDI-TOF conditions.

3.2. Crystal and Molecular Structures. The molecular structures of the ligands $H_2L^{Me_2}$ and $H_2L^{Cl_2}$ obtained by single-crystal X-ray diffraction are shown in Supporting Information, Figure S1 and are good references for the dinuclear oxo-bridged complexes. Single-crystals of $[L^{Me_2}Fe(\mu\text{-}O)FeL^{Me_2}]$ and $[L^{Cl_2}Fe(\mu\text{-}O)FeL^{Cl_2}]$ suitable for X-ray diffraction were obtained by slow evaporation of the reaction solvent. Recrystallization of $[L^{Cl_2}Fe(\mu\text{-}O)FeL^{Cl_2}]$ from CH_2Cl_2/ethanol yielded single-crystals of $[L^{Cl_2}Fe(\mu\text{-}O)FeL^{Cl_2}]\cdot CH_2Cl_2$ also suitable for X-ray diffraction.

The asymmetric unit of $[L^{Me_2}Fe(\mu\text{-}O)FeL^{Me_2}]$ incorporates two independent half molecules. Inversion centers at the oxo ions generate the complete molecules (molecule 1: Fe1 and Fe1′; molecule 2: Fe2 and Fe2′). The asymmetric units of $[L^{Cl_2}Fe(\mu\text{-}O)FeL^{Cl_2}]$ and $[L^{Cl_2}Fe(\mu\text{-}O)FeL^{Cl_2}]\cdot CH_2Cl_2$ each incorporate a complete molecule of $[L^{Cl_2}Fe(\mu\text{-}O)FeL^{Cl_2}]$.

The molecular structures of $[L^{Me_2}Fe(\mu\text{-}O)FeL^{Me_2}]$, $[L^{Cl_2}Fe(\mu\text{-}O)FeL^{Cl_2}]$, and of $[L^{Cl_2}Fe(\mu\text{-}O)FeL^{Cl_2}]\cdot CH_2Cl_2$ are shown in Figure 1, together with that of $[L^{t\text{-}Bu_2}Fe(\mu\text{-}O)FeL^{t\text{-}Bu_2}]$[42] for comparison. Thermal ellipsoid plots and numbering schemes are given in Supporting Information, Figures S2 and S3 for $[L^{Me_2}Fe(\mu\text{-}O)FeL^{Me_2}]$ and $[L^{Cl_2}Fe(\mu\text{-}O)FeL^{Cl_2}]$, respectively. Detailed listings of interatomic distances and angles are provided in Supporting Information, Tables S2−S6; a comparison of selected structural parameters is summarized in Table 1.

As in $[L^{t\text{-}Bu_2}Fe(\mu\text{-}O)FeL^{t\text{-}Bu_2}]$, the Fe^{III} ions in all complexes are five-coordinate, with a bridging oxo ion, resulting in a distorted square-pyramidal coordination polyhedron (τ-values[49] between 0.04 and 0.35, Table 1).

(49) Addison, A. W.; Rao, T. N.; Reedijk, J.; van Rijn, J.; Verschoor, G. C. *J. Chem. Soc., Dalton Trans.* **1984**, 1349–1356.

The donor atoms of the ligands $(L^{X_2})^{2-}$ form the basal planes and thus adopt *trans*-conformations in all complexes.[50] It is of interest to note that the conformation of the linear tetradentate ligand $(L^{X_2})^{2-}$ varies. For $[L^{t\text{-}Bu_2}Fe(\mu\text{-}O)FeL^{t\text{-}Bu_2}]$, one of the two methyl groups bound to the nitrogen atoms in each ligand is directed toward the bridging oxo ion, whereas the other methyl group is directed in the opposite direction. On the other hand, both of these methyl groups in each ligand of $[L^{Me_2}Fe(\mu\text{-}O)FeL^{Me_2}]$, $[L^{Cl_2}Fe(\mu\text{-}O)FeL^{Cl_2}]$, and $[L^{Cl_2}Fe(\mu\text{-}O)FeL^{Cl_2}]\cdot CH_2Cl_2$ are directed toward the oxo ion.

The molecular structures of the two independent molecules in $[L^{Me_2}Fe(\mu\text{-}O)FeL^{Me_2}]$ exhibit significant differences, which are easily visible from the relative orientations of the phenol rings (Figure 1b,c). Using $[L^{t\text{-}Bu_2}Fe(\mu\text{-}O)FeL^{t\text{-}Bu_2}]$ as reference with the phenol rings oriented almost coplanar to the O_2N_2-planes, in $[L^{Me_2}Fe(\mu\text{-}O)FeL^{Me_2}]$ molecule 1 shows some deviations and molecule 2 shows strong deviations. In both structures of $[L^{Cl_2}Fe(\mu\text{-}O)FeL^{Cl_2}]$, the phenol rings are more regularly oriented. These differences suggest that the relative orientations of the phenol rings and thus the $Fe-O^{Ph}$ bonding interactions have very flat potentials for rearrangement.

A striking difference is in the Fe−O−Fe angle, which are 180° for X = *t*-Bu and Me and 166.1° and 166.3° for the two complexes with X = Cl. In addition, $[L^{Cl_2}Fe(\mu\text{-}O)FeL^{Cl_2}]$ exhibits the strongest distortion to a trigonal-bipyramidyl coordination environment.

3.3. X-ray Absorption Spectroscopy. Fe K-edge X-ray absorption spectroscopy measurements have been performed on $[L^{t\text{-}Bu_2}Fe(\mu\text{-}O)FeL^{t\text{-}Bu_2}]$ as a solid in BN and in CH_2Cl_2 solution (Supporting Information, Figure S4), as a reference for the oxidized species (vide infra). The solid state Fe K-edge exhibits an intense pre-edge peak at 7113.6 eV consistent with a 5-coordinate oxo-bridged iron complex. This pre-edge feature is shifted to slightly higher energy of 7113.7 eV in the solution spectrum, with a slight decrease in intensity. Both spectra exhibit a rising edge inflection at 7123.4 eV. However, above the edge (in the 7127−7135 eV range) the spectra differ slightly. This may result from subtle changes of the structure in solution.

Because of the absorbing nature of the solvent (CH_2Cl_2) extended X-ray absorption fine structure (EXAFS) data with a sufficient signal-to-noise ratio could only be obtained to k = 12 Å^{-1} for the solution. The EXAFS data show significant differences between the solid-state and the solution, with clear changes in the overall beat pattern. Interestingly, in the Fourier transforms the broad peak at 1.5 Å in the solid state splits into two peaks in the solution data. These changes indicate that there are differences between the solid and solution states. Supporting Information, Table S7 summarizes the best fits to the data. It should be noted that the different bond lengths of the two different Fe−O components in the crystal structure (2 $Fe-O^{Ph}$ at 1.86 Å and 1 $Fe-O^{oxo}$ at 1.78 Å) were not resolved in the solid state spectrum. Three Fe−O components at 1.88 Å were required, and attempts to separate these components are beyond the resolution of the data. The same applies for the solution data despite the observed splitting in the Fourier transform. Three Fe−O contributions at slightly shorter distance of 1.86 Å were needed to model the data. The most significant difference in the two data sets is the Fe−N distance, which is 2.14 Å in solution as compared to 2.25 Å in the solid state. These distances are also slightly longer than the values of 2.21 and 2.24 Å obtained from single-crystal X-ray diffraction. The Fe−Fe distance at 3.55 Å in solution is slightly shorter than 3.59 Å in the solid state. In summary, the X-ray absorption spectroscopy (XAS) measurements indicate that the dinuclear complex $[L^{t\text{-}Bu_2}Fe(\mu\text{-}O)FeL^{t\text{-}Bu_2}]$ remains intact in CH_2Cl_2 solution (dissociation of a few percent of the complex are below the limits of this method) and that the complex exhibits some structural rearrangement in solution as compared to the solid state. This implies that some packing effects influence the molecular structure found by X-ray crystallography, which corroborates the assumption of flat potentials for rearrangement along some modes (vide supra).

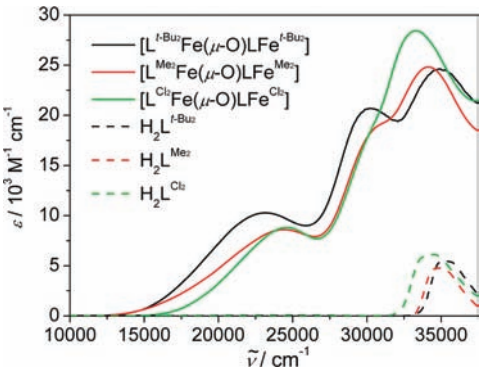

Figure 2. Electronic absorption spectra of $[L^{t\text{-}Bu_2}Fe(\mu\text{-}O)FeL^{t\text{-}Bu_2}]$, $[L^{Me_2}Fe(\mu\text{-}O)FeL^{Me_2}]$, $[L^{Cl_2}Fe(\mu\text{-}O)FeL^{Cl_2}]$, $H_2L^{t\text{-}Bu_2}$, $H_2L^{Me_2}$, and $H_2L^{Cl_2}$ in CH_2Cl_2 at 25 °C.

3.4. Electronic Absorption Spectroscopy. The UV−vis−NIR spectra of $[L^{t\text{-}Bu_2}Fe(\mu\text{-}O)FeL^{t\text{-}Bu_2}]$, $[L^{Me_2}Fe(\mu\text{-}O)FeL^{Me_2}]$, and $[L^{Cl_2}Fe(\mu\text{-}O)FeL^{Cl_2}]$ in CH_2Cl_2 solution are displayed in Figure 2 together with the spectra of the three ligands. The spectroscopic properties are summarized in Table 2. It should be noted that dissociation of $[L^{t\text{-}Bu_2}Fe(\mu\text{-}O)FeL^{t\text{-}Bu_2}]$ in solution can only be prevented by use of oxygen- and moisture-free CH_2Cl_2. If this is not accounted for, energies and intensities in the UV−vis spectrum may differ, as published previously.[42,43]

The spectra of $[L^{Me_2}Fe(\mu\text{-}O)FeL^{Me_2}]$ and $[L^{Cl_2}Fe(\mu\text{-}O)FeL^{Cl_2}]$ exhibit two absorption maxima in the range between 10000 and 38000 cm^{-1}, while the spectrum of $[L^{t\text{-}Bu_2}Fe(\mu\text{-}O)FeL^{t\text{-}Bu_2}]$[42] consists of three absorption maxima. Nevertheless, all three spectra may be divided into three absorption regions. The absorptions above 33000 cm^{-1} are mainly due to $\pi \rightarrow \pi^*$ transitions of the phenolic chromophores, which are also present in the three ligands. The low energy features in the 15000−25000 cm^{-1} region can mainly be assigned to $p_\pi \rightarrow d_{\pi^*}$ charge transfer (CT) transitions of the phenolic ligands and some weaker oxo-to-iron CT transitions. Around 30000 cm^{-1} strong absorptions with main character of $p_\pi \rightarrow d_{\sigma^*}$ phenolate ligand-to-metal charge transfer

(50) Selbin, J.; Bailar, J. C., Jr. *J. Am .Chem. Soc.* **1960**, *82*, 1524–1526.

Table 2. Spectroscopic and Magnetic Properties of [$L^{t\text{-}Bu_2}Fe(\mu\text{-}O)FeL^{t\text{-}Bu_2}$], [$L^{Me_2}Fe(\mu\text{-}O)FeL^{Me_2}$], and [$L^{Cl_2}Fe(\mu\text{-}O)FeL^{Cl_2}$]

	[$L^{t\text{-}Bu_2}Fe(\mu\text{-}O)FeL^{t\text{-}Bu_2}$]	[$L^{Me_2}Fe(\mu\text{-}O)FeL^{Me_2}$]	[$L^{Cl_2}Fe(\mu\text{-}O)FeL^{Cl_2}$][a]	
$\tilde{\nu}$/ cm^{-1} ε/M^{-1} cm^{-1}	23200 (10300)	24400 (8600)	24600 (8800)	
	30200 (20700)	30900 (19100)[b]	30900 (19100)[b]	
	35000 (24600)	34200 (24800)	33300 (28400)	
J/cm^{-1}	-89 ± 2	-98 ± 2	-100 ± 3	-99 ± 2
g_i	1.99	2.00	2.00	2.00
p.i./%	1.2	0.9	2.3	0.85
θ_w (p.i.)/K[d]	-3.8	-1.2	-9.0	0
δ/mm s^{-1}	0.44	0.44	0.42	0.42
$\lvert\Delta E_Q\rvert$/mm s^{-1}	1.22	1.23	0.89	1.01
Γ/mm s^{-1}	0.32	0.27	0.30	0.31
$E^1_{p,red}$/V vs Fc^+/Fc	-2.05	-1.75		-1.30
$E^2_{1/2}$/V vs Fc^+/Fc	$+0.27$	$+0.29$[c]		$+0.87$[c]
$E^3_{1/2}$/V vs Fc^+/Fc	$+0.44$	$+0.49$[c]		$+0.98$[c]

[a] Left values for crystals of [$L^{Cl_2}Fe(\mu\text{-}O)FeL^{Cl_2}$], right values for crystals of [$L^{Cl_2}Fe(\mu\text{-}O)FeL^{Cl_2}$]·$CH_2Cl_2$. [b] Shoulder. [c] Extracted from the fast scan rate experiments as the mid points of the oxidative and reductive peak maxima; it must be noted that these are not reversible ET waves. [d] The low-temperature decline of the paramagnetic impurity (p.i.) contribution below 10 K was modeled by assuming intermolecular interaction of the p.i. contributions.

(LMCT) transition are present.[42,51−54] The phenolate LMCT transitions are at lower energies in [$L^{t\text{-}Bu_2}Fe(\mu\text{-}O)FeL^{t\text{-}Bu_2}$] compared to the other two complexes, resulting in an overlap with the $\pi \rightarrow \pi^*$ transitions in [$L^{Me_2}Fe(\mu\text{-}O)FeL^{Me_2}$] and [$L^{Cl_2}Fe(\mu\text{-}O)FeL^{Cl_2}$]. Therefore, the LMCT transitions for these two complexes appear only as shoulders.

3.5. Magnetic Susceptibility. The effective magnetic moments, μ_{eff}, of [$L^{t\text{-}Bu_2}Fe(\mu\text{-}O)FeL^{t\text{-}Bu_2}$],[42] [$L^{Me_2}Fe(\mu\text{-}O)FeL^{Me_2}$], [$L^{Cl_2}Fe(\mu\text{-}O)FeL^{Cl_2}$] (Supporting Information, Figure S5), and [$L^{Cl_2}Fe(\mu\text{-}O)FeL^{Cl_2}$]·$CH_2Cl_2$ decrease with decreasing temperatures. This behavior is typical for an antiferromagnetic coupling of two Fe^{III} high-spin ions with $S_t = 0$ ground state. Furthermore, the measurements exhibit a plateau of μ_{eff} between 15 and 50 K, which can be ascribed to traces of a paramagnetic impurity.

Spin-Hamiltonian simulations of the magnetic properties using $S_i = 5/2$ for both ferric ions (eq 1 in the Supporting Information) reproduce the experimental data well. The coupling constants J, the g_i values, and the contributions of paramagnetic impurities (p. i.) are summarized in Table 2. The coupling constants are found in a range typical for oxo-bridged dinuclear Fe^{III} complexes,[55−57] with the antiferromagnetic coupling in [$L^{t\text{-}Bu_2}Fe(\mu\text{-}O)FeL^{t\text{-}Bu_2}$] being significantly smaller than in [$L^{Me_2}Fe(\mu\text{-}O)FeL^{Me_2}$] and [$L^{Cl_2}Fe(\mu\text{-}O)FeL^{Cl_2}$].

3.6. Mössbauer Spectroscopy. The solid state ^{57}Fe Mössbauer spectra at 80 K (Figure 3) exhibit quadrupole doublets with values provided in Table 2. The low isomer shifts of 0.42 to 0.44 mm s^{-1} are consistent with high-spin ferric ions with strong covalent metal−ligand interactions. The quadrupole splittings of 0.89 to 1.23 mm s^{-1} are relatively low for μ-oxo-bridged diiron complexes, which generally fall in the range 1.5 to 2.0 mm s^{-1}.[51] The corresponding high electric field-gradient arises from the short Fe−O^{oxo} bond distance (~ 1.7 to 1.8 Å), which leads to a pronounced anisotropy in the covalency. However,

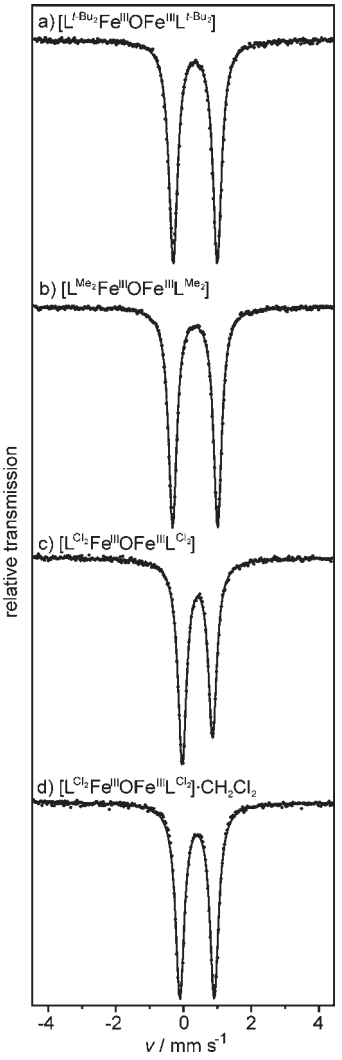

Figure 3. Solid-state Mössbauer spectra of (a) [$L^{t\text{-}Bu_2}Fe(\mu\text{-}O)FeL^{t\text{-}Bu_2}$], (b) [$L^{Me_2}Fe(\mu\text{-}O)FeL^{Me_2}$], (c) [$L^{Cl_2}Fe(\mu\text{-}O)FeL^{Cl_2}$], and (d) [$L^{Cl_2}Fe(\mu\text{-}O)FeL^{Cl_2}$]·$CH_2Cl_2$ recorded at 80 K. The solid lines correspond to simulations with parameters provided in Table 2. The line asymmetry in (c) is simulated by allowing for different widths of the low- and the high-energy lines of the doublet, keeping the intensities/areas equal (ratio of line widths 0.7:1).

(51) Que, L. *Prog. Inorg. Chem.* **1990**, *38*, 97.
(52) Brown, C. A.; Remar, G. J.; Musselman, R. L.; Solomon, E. I. *Inorg. Chem.* **1995**, *34*, 688–717.
(53) Karpishin, T. B.; Gebhard, M. S.; Solomon, E. I.; Raymond, K. N. *J. Am. Chem. Soc.* **1991**, *113*, 2977–2984.
(54) Davis, M. I.; Orville, A. M.; Neese, F.; Zaleski, J. M.; Lipscomb, J. D.; Solomon, E. I. *J. Am. Chem. Soc.* **2002**, *124*, 602–614.
(55) Gorun, S. M.; Lippard, S. J. *Inorg. Chem.* **1991**, *30*, 1625–1630.
(56) Weihe, H.; Güdel, H. U. *J. Am. Chem. Soc.* **1997**, *119*, 6539–6543.
(57) Norman, R. E.; Holz, R. C.; Menage, S.; O'Connor, C. J.; Zhang, J. H.; Que, L., Jr. *Inorg. Chem.* **1990**, *29*, 4629–4637.

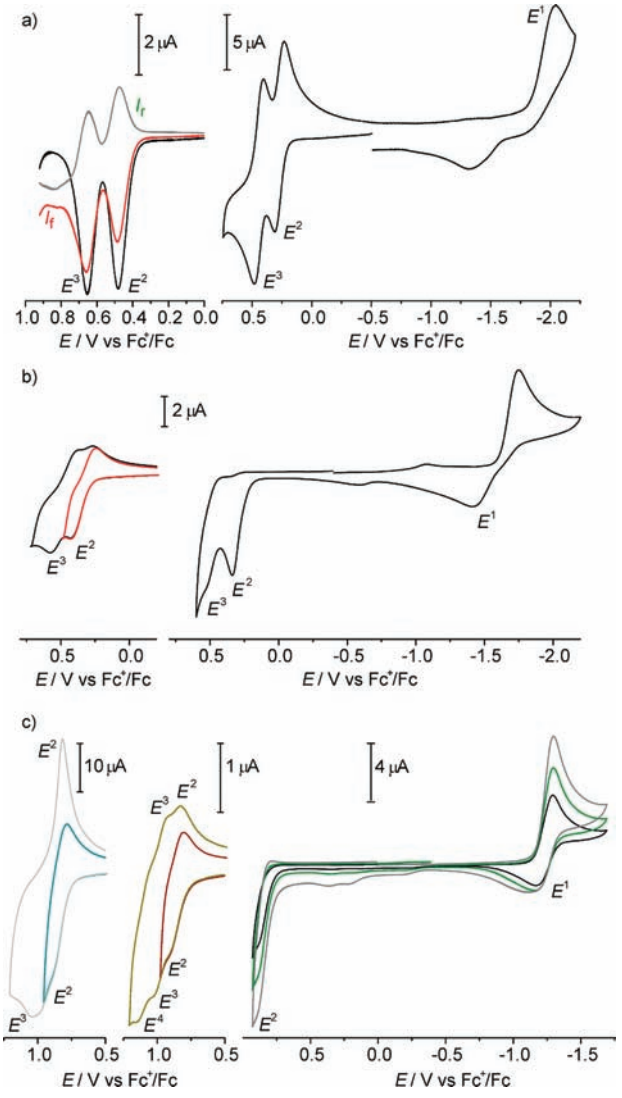

Figure 4. Electrochemistry of (a) [$L^{t\text{-}Bu_2}Fe(\mu\text{-}O)FeL^{t\text{-}Bu_2}$],[43] (b) [$L^{Me_2}Fe(\mu\text{-}O)FeL^{Me_2}$], and (c) [$L^{Cl_2}Fe(\mu\text{-}O)FeL^{Cl_2}$] in CH_2Cl_2 (0.2 M[$(n\text{-}Bu)_4N$](PF_6). Conditions: (a) SW: frequency: 20 Hz, $T = -40$ °C, GC WE; CV: scan rate: 100 mV s^{-1}, −40 °C, GC WE. (b) SW: scan rate: 40 V s^{-1}, 20 °C, Pt microWE; CV: scan rate: 100 mV s^{-1}, GC WE; (c) left: scan rate: 1 V s^{-1}, −25 °C, Pt microWE; center: scan rate: 10 V s^{-1}, 20 °C, Pt microWE; right: scan rates: 50, 100, 200 mV s^{-1}, 20 °C, GC WE.

we have shown in the study of the mononuclear complexes of the ligand $H_2L^{t\text{-}Bu_2}$ that the strong quadrupole splitting of 1.24 mm s^{-1} for [$L^{t\text{-}Bu_2}FeCl$] arises from strong covalent and highly anisotropic $Fe-O^{Ph}$ bonding interactions.[41] Therefore, the competing oxo and phenolate bonding interactions to the iron might be responsible for the relatively low quadrupole splittings in these oxo-bridged diiron complexes.

3.7. Electrochemistry. Cyclic voltammograms (CVs) and square-wave voltammograms (SWs) of [$L^{Me_2}Fe(\mu\text{-}O)FeL^{Me_2}$] and [$L^{Cl_2}Fe(\mu\text{-}O)FeL^{Cl_2}$] are shown in Figure 4 and potentials are provided in Table 2. Analogous data for [$L^{t\text{-}Bu_2}Fe(\mu\text{-}O)FeL^{t\text{-}Bu_2}$] are also provided for comparison.[43]

The CVs at 100 mV s^{-1} exhibit a reductive wave E^1 in the range −1.30 to −2.05 V (Table 2). The appearance of an oxidative wave depends on the conditions chosen for the respective measurement. However, these reductions are not electrochemically reversible.

All three complexes exhibit a first oxidative wave E^2 at a scan rate of 100 mV s^{-1} in the CVs. The peak potentials are 0.31, 0.34, and ∼0.9 V for [$L^{t\text{-}Bu_2}Fe(\mu\text{-}O)FeL^{t\text{-}Bu_2}$], [$L^{Me_2}Fe(\mu\text{-}O)FeL^{Me_2}$], and [$L^{Cl_2}Fe(\mu\text{-}O)FeL^{Cl_2}$], respectively. Only the complex of the *t*-Bu substituted ligand exhibits a reductive wave at these conditions, indicative of a reversible oxidation. This first oxidation results in the formation of the monocationic complexes. While [$L^{Me_2}Fe(\mu\text{-}O)FeL^{Me_2}]^+$ and [$L^{Cl_2}Fe(\mu\text{-}O)FeL^{Cl_2}]^+$ are unstable on the time-scale of this experiment, [$L^{t\text{-}Bu_2}Fe(\mu\text{-}O)FeL^{t\text{-}Bu_2}]^+$ appears to be stable. By increasing the scan rates of the CVs, a reductive peak appears for [$L^{Me_2}Fe(\mu\text{-}O)FeL^{Me_2}$] and [$L^{Cl_2}Fe(\mu\text{-}O)FeL^{Cl_2}$]. In the case of [$L^{Me_2}Fe(\mu\text{-}O)FeL^{Me_2}$], a scan rate of 40 V s^{-1} at 20 °C has to be used, although the peak current ratio I_{red}/I_{ox} is still below 1. In the case of [$L^{Cl_2}Fe(\mu\text{-}O)FeL^{Cl_2}$] a scan rate of 10 V s^{-1} at 20 °C or 1 V s^{-1} at −25 °C results in the appearance of the reductive peak with a peak current ratio I_{red}/I_{ox} of almost 1.

These observations establish that at high scan-rates the re-reductions of the monocations, [$L^{Me_2}Fe(\mu\text{-}O)FeL^{Me_2}]^+$ and [$L^{Cl_2}Fe(\mu\text{-}O)FeL^{Cl_2}]^+$, compete kinetically with a relatively fast chemical reaction of the monocations. The half-life $\tau_{1/2}$ can be estimated from the CVs from the time span between the oxidative and the reductive peak to be ∼9 ms at 20 °C for the monocation [$L^{Me_2}Fe(\mu\text{-}O)FeL^{Me_2}]^+$ and ∼0.7 s at −25 °C for [$L^{Cl_2}Fe(\mu\text{-}O)FeL^{Cl_2}]^+$.

The CVs at a scan-rate of 100 mV s^{-1} exhibit a second oxidative wave E^3 with peak potentials in the range of 0.48 and to ∼1.1 V. However, only the CV of [$L^{t\text{-}Bu_2}Fe(\mu\text{-}O)FeL^{t\text{-}Bu_2}$] exhibits an intensive reductive peak with a peak potential difference of 0.08 V. This is indicative of a reversible oxidation with $E^3{}_{1/2} = 0.44$ V, which is corroborated by the SW measurements. The line width of E^2 and E^3 and the peak currents closely resemble. Therefore, this second oxidation E^3 should be assigned to a reversible oxidation of the monocation [$L^{t\text{-}Bu_2}Fe(\mu\text{-}O)FeL^{t\text{-}Bu_2}]^+$ to the dication [$L^{t\text{-}Bu_2}Fe(\mu\text{-}O)FeL^{t\text{-}Bu_2}]^{2+}$.

3.8. Spectro-Electrochemistry of [$L^{t\text{-}Bu_2}Fe(\mu\text{-}O)FeL^{t\text{-}Bu_2}$]. A controlled potentiostatic coulometry at −40 °C was performed at a potential of 0.39 V and followed by UV−vis spectroscopy (Figure 5a). The UV−vis spectra exhibit almost isosbestic behavior for the first 50% of the charge necessary for a one-electron oxidation (isosbestic points at 21500 cm^{-1} and 23400 cm^{-1}). The extinction at 24000 cm^{-1} increases with a shift of the absorption maximum from 23400 to 24100 cm^{-1}. Additionally, a broad absorption centered around 17000 cm^{-1} appears. After this, the behavior becomes non-isosbestic, indicating a chemical reaction of the electrochemically generated [$L^{t\text{-}Bu_2}Fe(\mu\text{-}O)FeL^{t\text{-}Bu_2}]^+$. Several more measurements at varying temperatures and concentrations exhibit the same qualitative behavior. Samples for EPR spectroscopy were taken during several measurements after varying time intervals and were directly frozen in liquid nitrogen. All EPR spectra consist of an isotropic $S = 1/2$ spectrum with g values in the range 2.0044 to 2.0050. A representative EPR spectrum is shown in Supporting Information, Figure S6. The spin concentration was determined for these samples and related to the consumed charge. This relative spin concentration is higher for samples taken after short times in comparison to samples taken after longer times. For example, the spin concentration of an EPR sample prepared by coulometry at −40 °C

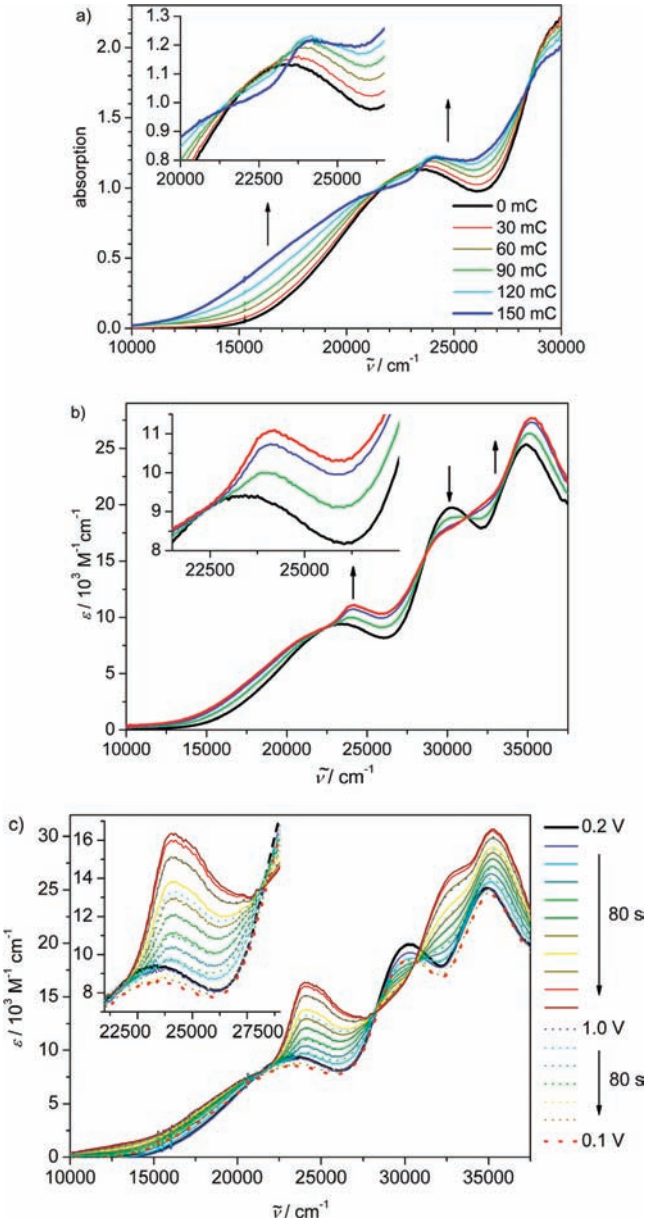

Figure 5. (a) UV−vis spectra recorded during a potentiostatic coulometry of [$L^{t\text{-}Bu_2}$Fe(μ-O)Fe$L^{t\text{-}Bu_2}$] at −40 °C in CH_2Cl_2 (0.2 M [(n-Bu_4)N](PF_6)) at a fixed potential of +0.39 V vs Fc^+/Fc (188 mC required for a one-electron oxidation). (b) UV−vis spectra recorded during a CV of [$L^{t\text{-}Bu_2}$Fe(μ-O)Fe$L^{t\text{-}Bu_2}$] in CH_2Cl_2 in an OTTLE cell at −20 °C. Scanrate: 3 mV s^{-1}. Spectra recorded at: 0.16 V (black), 0.24 V (red), 0.32 V (green), 0.40 V vs Fc^+/Fc (blue). (c) UV−vis spectra recorded during a chronoamperometry of [$L^{t\text{-}Bu_2}$Fe(μ-O)Fe$L^{t\text{-}Bu_2}$] in CH_2Cl_2 in an OTTLE cell at −20 °C.

performed to 80% of a theoretical one-electron oxidation, corresponds to 86% of the compound present.

The time-scale of these bulk coulometry experiments (~30 min) does not allow to generate a clean sample of oxidized [$L^{t\text{-}Bu_2}$Fe(μ-O)Fe$L^{t\text{-}Bu_2}$]$^+$, as this oxidized species decays on this time-scale. Therefore, the formation of [$L^{t\text{-}Bu_2}$Fe(μ-O)Fe$L^{t\text{-}Bu_2}$]$^+$ was followed by UV−vis spectroscopy during a CV in an OTTLE cell at −20 °C (Figure 5b), which took roughly 2 min. As seen in the bulk coulometry, a new band at 24100 cm^{-1} arises, associated with clear isosbestic points at 22500, 28700, and 31200 cm^{-1}. Because of the isosbestic behavior, the last spectrum

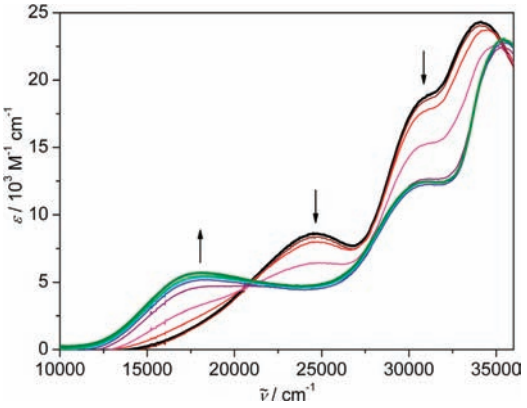

Figure 6. UV−vis spectra recorded during a CV of [L^{Me_2}Fe(μ-O)FeL^{Me_2}] in CH_2Cl_2 in an OTTLE cell at −20 °C. Scan rate: 3 mV s^{-1}. Selected spectra taken at the starting potential of −0.83 V (black), the turning point of 0.35 V (green), and the final potential of −0.83 V vs Fc^+/Fc (blue). The oxidation scan took 60 s as did the reductive scan.

taken at 0.40 V can be assigned to the spectrum of pure [$L^{t\text{-}Bu_2}$Fe(μ-O)Fe$L^{t\text{-}Bu_2}$]$^+$.

To test the reversibility of the second oxidation, a chronoamperometry in CH_2Cl_2 at −20 °C in an OTTLE cell was performed and followed by UV−vis spectroscopy (Figure 5c). A strong intensity increase at 24100 cm^{-1} occurs. Additionally, the extinction decreases at 30100 cm^{-1} and increases at 35200 cm^{-1}. It can be assumed that the monocation [$L^{t\text{-}Bu_2}$Fe(μ-O)Fe$L^{t\text{-}Bu_2}$]$^+$ and the dication [$L^{t\text{-}Bu_2}$Fe(μ-O)Fe$L^{t\text{-}Bu_2}$]$^{2+}$ are both present. In this respect, the continuity of the changes in the UV−vis spectra and the relatively well-defined isosbestic points imply similar electronic processes for the generation of the monocation [$L^{t\text{-}Bu_2}$Fe(μ-O)Fe$L^{t\text{-}Bu_2}$]$^+$ and the dication [$L^{t\text{-}Bu_2}$Fe(μ-O)Fe$L^{t\text{-}Bu_2}$]$^{2+}$. It should be noted that during the re-reduction of the dication $L^{t\text{-}Bu_2}$Fe(μ-O)Fe$L^{t\text{-}Bu_2}$]$^{2+}$, the spectrum of the neutral starting complex [$L^{t\text{-}Bu_2}$Fe(μ-O)Fe$L^{t\text{-}Bu_2}$] is almost completely restored, demonstrating that this two-electron oxidation is almost reversible on this time-scale. Only a small amount of oxidized product undergoes further chemical reactions.

3.9. Spectro-Electrochemistry of [L^{Me_2}Fe(μ-O)FeL^{Me_2}]. The oxidation of a CH_2Cl_2 solution of [L^{Me_2}Fe(μ-O)FeL^{Me_2}] at −20 °C in an OTTLE cell was followed by UV−vis spectroscopy (Figure 6). During the oxidative scan, the absorption maximum at 24400 cm^{-1} disappeared, and a new maximum at 18000 cm^{-1} appeared in the spectrum. During the reduction scan, only slight changes appeared in the spectra. The spectrum of the neutral starting material [L^{Me_2}Fe(μ-O)FeL^{Me_2}] is not restored. This establishes that the oxidized species [L^{Me_2}Fe(μ-O)FeL^{Me_2}]$^+$ is not stable on the time-scale of this experiment in agreement with the result of the CV measurements.

3.10. Chemical Oxidations of [$L^{t\text{-}Bu_2}$Fe(μ-O)Fe$L^{t\text{-}Bu_2}$]. The electrochemical and spectroelectrochemical investigations showed that the monocation [$L^{t\text{-}Bu_2}$Fe(μ-O)Fe$L^{t\text{-}Bu_2}$]$^+$ and the dication [$L^{t\text{-}Bu_2}$Fe(μ-O)Fe$L^{t\text{-}Bu_2}$]$^{2+}$ are intermediate species with lifetimes that should be sufficiently long for characterization at low temperatures. To study the electronic structures and the decay reactions, we have generated these species at low temperatures by chemical oxidation. The electronic structures were probed by UV−vis, X-ray absorption, and Mössbauer spectroscopy in

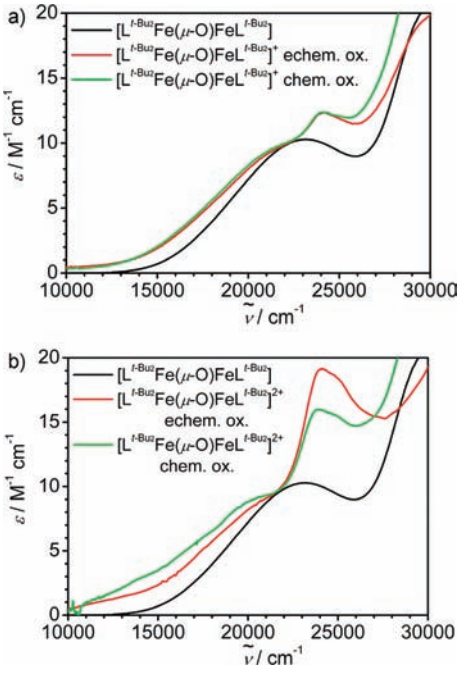

Figure 7. (a) Comparison of UV−vis spectra of chemically generated $[L^{t\text{-Bu}_2}Fe(\mu\text{-O})FeL^{t\text{-Bu}_2}]^+$ (−55 °C), electrochemically generated $[L^{t\text{-Bu}_2}Fe(\mu\text{-O})FeL^{t\text{-Bu}_2}]^+$ (−20 °C), and the starting material $[L^{t\text{-Bu}_2}Fe(\mu\text{-O})FeL^{t\text{-Bu}_2}]$ (room temperature) in CH_2Cl_2. The spectrum of the chemically oxidized monocation includes the absorption of 1 equiv of the reduced **AR**, which exhibits strong absorptions above 25000 cm^{-1}. (b) Comparison of the UV−vis spectra of the chemically generated dication $[L^{t\text{-Bu}_2}Fe(\mu\text{-O})FeL^{t\text{-Bu}_2}]^{2+}$ (−40 °C), the electrochemically generated dication $[L^{t\text{-Bu}_2}Fe(\mu\text{-O})FeL^{t\text{-Bu}_2}]^{2+}$ (−20 °C), and the neutral $[L^{t\text{-Bu}_2}Fe(\mu\text{-O})FeL^{t\text{-Bu}_2}]$ (room temperature) in CH_2Cl_2. The spectrum of the chemically oxidized dication includes the absorption of 2 equiv of the reduced **AR**, which exhibits strong absorption above 25000 cm^{-1}.

solution. Time-dependent studies and the identification of the final products allowed the investigation of the decay reactions.

The choice of the experimental conditions was rather limited. $[L^{t\text{-Bu}_2}Fe(\mu\text{-O})FeL^{t\text{-Bu}_2}]$ shows sufficient solubility without decomposition only in CH_2Cl_2. Thus, the oxidant should be soluble in CH_2Cl_2 and oxidize $[L^{t\text{-Bu}_2}Fe(\mu\text{-O})FeL^{t\text{-Bu}_2}]$ quickly. The aminyl radical $((C_6H_4Br)_3N)(SbCl_6)$ (**AR**) combines the required solubility in CH_2Cl_2 with a redox potential of 0.9 V versus Fc^+/Fc suited for both oxidations of $[L^{t\text{-Bu}_2}Fe(\mu\text{-O})FeL^{t\text{-Bu}_2}]$.[58] The experimental conditions for analysis by UV−vis, X-ray absorption, and Mössbauer spectroscopies were chosen as similar as possible.

Addition of 1 equiv of **AR** to $[L^{t\text{-Bu}_2}Fe(\mu\text{-O})FeL^{t\text{-Bu}_2}]$ results in a new UV−vis spectrum (Figure 7a), whose generation is too fast to be followed by our experimental setup at all temperatures studied. The absorption maximum of $[L^{t\text{-Bu}_2}Fe(\mu\text{-O})FeL^{t\text{-Bu}_2}]$ shifts from 23400 cm^{-1} to 24100 cm^{-1} with an increase in the intensity. This spectrum closely resembles the spectrum obtained by electrochemical one-electron oxidation. It must be noted that the **AR** oxidant converts to the neutral amine $(C_6H_4Br)_3N$. This exhibits a strong absorption feature at 32600 cm^{-1} with $\varepsilon = 26300$ M^{-1} cm^{-1}, and even below 30000 cm^{-1} the intensity is still 9000 M^{-1} cm^{-1} Thus, the intensities provided in Figure 7a above 25000 cm^{-1} may be severely obscured. However, the spectrum of the chemically generated monocation $[L^{t\text{-Bu}_2}Fe(\mu\text{-O})FeL^{t\text{-Bu}_2}]^+$ deviates slightly from that of the electrochemically generated one also around 18000 cm^{-1}, showing some intensity that is not present for the latter. This is a common feature of all oxidations performed with 1 equiv of **AR** irrespective of the temperature.

This behavior is even more pronounced in the UV−vis spectra of the two-electron oxidized $[L^{t\text{-Bu}_2}Fe(\mu\text{-O})FeL^{t\text{-Bu}_2}]^{2+}$ (Figure 7b). Addition of 2 equiv of **AR** to $[L^{t\text{-Bu}_2}Fe(\mu\text{-O})FeL^{t\text{-Bu}_2}]$ results in a new species with an absorption maximum at 23900 cm^{-1}. The intensities above 25000 cm^{-1} incorporate the strong absorption features of 2 equiv of $(C_6H_4Br)_3N$. Although the new strong absorption at 23900 cm^{-1} with a shoulder at 24900 cm^{-1} closely resembles that of the electrochemically generated species, the intensity is significantly lower, whereas the broad maximum around 18000 cm^{-1} exhibits a slightly higher intensity. As several spectra recorded at different reaction times and different temperatures exhibit this feature, these differences are not due to an incomplete oxidation to the dication $[L^{t\text{-Bu}_2}Fe(\mu\text{-O})FeL^{t\text{-Bu}_2}]^{2+}$.

We assign the differences in the spectra of the chemically and the electrochemically generated oxidized species to chemical differences in the respective solutions. The oxidant chosen, $((C_6H_4Br)_3N)(SbCl_6)$, converts upon oxidation to the amine $(C_6H_4Br)_3N$ and the counterion $SbCl_6^-$, which are present in stoichiometric amounts. On the other hand, in the electrochemical solutions, a 200-fold excess of $[(n\text{-Bu})_4N]$ is present. Simply because of electrostatic attractions in CH_2Cl_2 solution, the formation of contact ion pairs is very likely.[59−62] Additionally, while the electron density at the Fe^{III} ions in the neutral species is sufficient for the five-coordinate square-pyramidal structure, the oxidation of the phenolates to phenoxyl radicals reduces the electron density of the ligands. As a consequence, the electron density of the Fe^{III} ions is reduced, which increases the tendency to form six-coordinate species. This assumption is corroborated by the analysis of the final products of the decay reactions and by the non-negligible value of the activation entropy (vide infra).

The starting material $[L^{t\text{-Bu}_2}Fe(\mu\text{-O})FeL^{t\text{-Bu}_2}]$ and the chemically generated monocation $[L^{t\text{-Bu}_2}Fe(\mu\text{-O})FeL^{t\text{-Bu}_2}]^+$ and dication $[L^{t\text{-Bu}_2}Fe(\mu\text{-O})FeL^{t\text{-Bu}_2}]^{2+}$ were studied by XAS in CH_2Cl_2 solution (Figure 8a). The Fe K-edge rising edge inflections are between 7123.4 and 7123.6 eV for all three complexes. The pre-edges show one strong absorption feature with a maximum at 7113.6−7113.7 eV. The small differences clearly rule out any iron-based oxidation; the close resemblance of the three spectra is even unexpected for ligand-based oxidations affording one and two coordinated phenoxyl radicals.

However, interestingly the EXAFS spectra (Figure 8b) of the monocation $[L^{t\text{-Bu}_2}Fe(\mu\text{-O})FeL^{t\text{-Bu}_2}]^+$ and the dication $[L^{t\text{-Bu}_2}Fe(\mu\text{-O})FeL^{t\text{-Bu}_2}]^{2+}$ differ significantly from the spectrum of the starting neutral complex $[L^{t\text{-Bu}_2}Fe(\mu\text{-O})FeL^{t\text{-Bu}_2}]$,

(58) Schmidt, W.; Steckhan, E. *Chem. Ber.* **1980**, *113*, 577–585.

(59) Winstein, S.; Clippinger, E.; Fainberg, A. H.; Robinson, G. C. *J. Am . Chem. Soc.* **1954**, *76*, 2597–2598.

(60) (a) Szwarc, M. *Acc. Chem. Res.* **1969**, *2*, 87–96. (b) Marcus, Y.; Hefter, G. *Chem. Rev.* **2006**, *106*, 4585–4621.

(61) Gutmann, V. *Coord. Chem. Rev.* **1976**, *18*, 225–255.

(62) Lambert, C.; von Ragué Schleyer, P. *Angew. Chem., Int. Ed.* **1994**, *33*, 1129–1140.

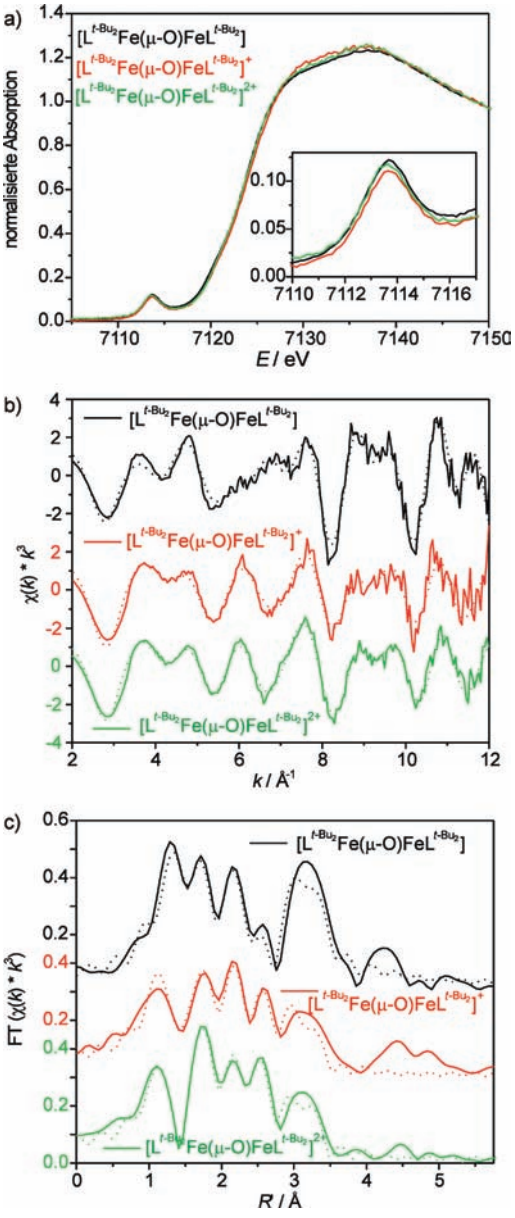

Figure 8. Comparison of XAS results of [$L^{t\text{-}Bu_2}$Fe(μ-O)Fe$L^{t\text{-}Bu_2}$], [$L^{t\text{-}Bu_2}$Fe(μ-O)Fe$L^{t\text{-}Bu_2}$]$^+$, and [$L^{t\text{-}Bu_2}$Fe(μ-O)Fe$L^{t\text{-}Bu_2}$]$^{2+}$ in CH_2Cl_2 solution: (a) Fe K-edges, (b) EXAFS spectra, and (c) the corresponding non-phase shift corrected Fourier transforms. The dotted lines in (b) and (c) correspond to the simulations.

especially in the region around $k \approx 6$ Å^{-1}, whereas the spectra of the mono- and the dication are again very similar (Figure 8b). Differences in the Fourier transforms (Figure 8c) are apparent in the range 1−2 Å^{-1} and 3−3.5 Å^{-1}. The best fits to the solution data are summarized in Supporting Information, Table S2.

The best fit to [$L^{t\text{-}Bu_2}$Fe(μ-O)Fe$L^{t\text{-}Bu_2}$] in solution results in 3 Fe−O distances of 1.86 Å, which account for the Fe−O^{Ph} as well as the Fe−O^{oxo} bonds. While the resolution of the data is not sufficient to resolve these distances, these two different bond lengths can be resolved in the data of the monocation [$L^{t\text{-}Bu_2}$Fe(μ-O)Fe$L^{t\text{-}Bu_2}$]$^+$ and the dication [$L^{t\text{-}Bu_2}$Fe(μ-O)Fe$L^{t\text{-}Bu_2}$]$^{2+}$. For both complexes, one short Fe−O vector at 1.78 Å and one Fe−O vector at 1.98 (monocation) or 1.99 Å (dication) were found. The former is assigned to the bridging oxo-ion, and the latter is assigned to the two Fe−O^{Ph} bond lengths. Interestingly, the Fe−Fe distance decreases from 3.55 Å in the neutral complex to 3.51 Å in the monocation and 3.50 Å in the dication.

Additional independent information on the oxidized species was derived from ^{57}Fe Mössbauer spectroscopy. This was a challenge because only CH_2Cl_2 could be used as solvent (see above) and chlorine affords strong mass absorption of 14 KeV γ-rays, so that samples with chlorinated solvents in general are opaque for Mössbauer radiation. However, with 100% ^{57}Fe-enriched compounds and optimized absorber thickness, obtained by elaborate thinning of the frozen samples to about 1 mm (see Experimental Section), the accumulation time could be reduced to the order of 3−4 weeks with acceptable signal-to-noise ratio. This allowed us at least to study the two-electron oxidized species [$L^{t\text{-}Bu_2}$Fe(μ-O)Fe$L^{t\text{-}Bu_2}$]$^{2+}$.

As expected for a symmetric dimer, starting material [$L^{t\text{-}Bu_2}$Fe(μ-O)Fe$L^{t\text{-}Bu_2}$] at 80 K exhibits a single Mössbauer quadrupole doublet in the solid state (Figure 3a) as well as in a concentrated CH_2Cl_2 solution (6.77 mM, Figure 9a). While the isomer shift is 0.44 mm s^{-1} for both spectra, the quadrupole splitting is 1.22 mm s^{-1} in the solid but 1.32 mm s^{-1} in solution in agreement with the structural rearrangements observed by EXAFS.

Because of the limiting solubility of the oxidant **AR**, the samples prepared for the chemical oxidation had to be of lower concentration (c = 2.99 mM). Two equivalents of **AR** were added to a CH_2Cl_2 solution of [$L^{t\text{-}Bu_2}$Fe(μ-O)Fe$L^{t\text{-}Bu_2}$] at −30 °C. After stirring for 15 min, the solution was frozen with liquid nitrogen. The Mössbauer spectrum of that sample again shows a unique quadrupole doublet revealing two identical iron sites, now with isomer shift 0.47 mm s^{-1} and quadrupole splitting 1.32 mm s^{-1} (Figure 9b). The slight increase in the isomer shift compared to the neutral complex indicates slightly less covalent bonding and thus less charge donation of the oxidized ligands.

3.11. Time- And Temperature-Dependent Studies on Oxidized [$L^{t\text{-}Bu_2}$Fe(μ-O)Fe$L^{t\text{-}Bu_2}$]$^+$ and [$L^{t\text{-}Bu_2}$Fe(μ-O)Fe$L^{t\text{-}Bu_2}$]$^{2+}$. 3.11.1. [$L^{t\text{-}Bu_2}$Fe(μ-O)Fe$L^{t\text{-}Bu_2}$]$^+$. Solutions of [$L^{t\text{-}Bu_2}$Fe(μ-O)Fe$L^{t\text{-}Bu_2}$]$^+$ were generated by addition of 1 equiv of **AR** to [$L^{t\text{-}Bu_2}$Fe(μ-O)Fe$L^{t\text{-}Bu_2}$] in CH_2Cl_2 at temperatures between −30 °C and −60 °C, and followed by electronic absorption spectroscopy. The qualitative changes in the spectra are almost identical for all temperatures measured. A typical example is provided in Figure 10. The characteristic absorption of the monocation at 24100 cm^{-1} decreases, while a new maximum at 17500 cm^{-1} appears. These changes are not associated with a clean isosbestic point but there is an almost isosbestic point at 20000 cm^{-1} for the first 20 min, which moves to 19300 cm^{-1} thereafter.

The spectra reveal that not only one decay reaction occurs, but that a second slower decay reaction is also present. We have fitted the time dependence of the increase of the band at 17250 cm^{-1} and the decrease of the band at 24100 cm^{-1} to a first order reaction. However, we have used two exponentials, as the second exponential mimics the onset of the second decay reaction (fits in Supporting Information, Figure S7, rate constants in Supporting Information, Table S8). The monocation [$L^{t\text{-}Bu_2}$Fe(μ-O)Fe$L^{t\text{-}Bu_2}$]$^+$ has a half-live of 27 min at −40 °C.

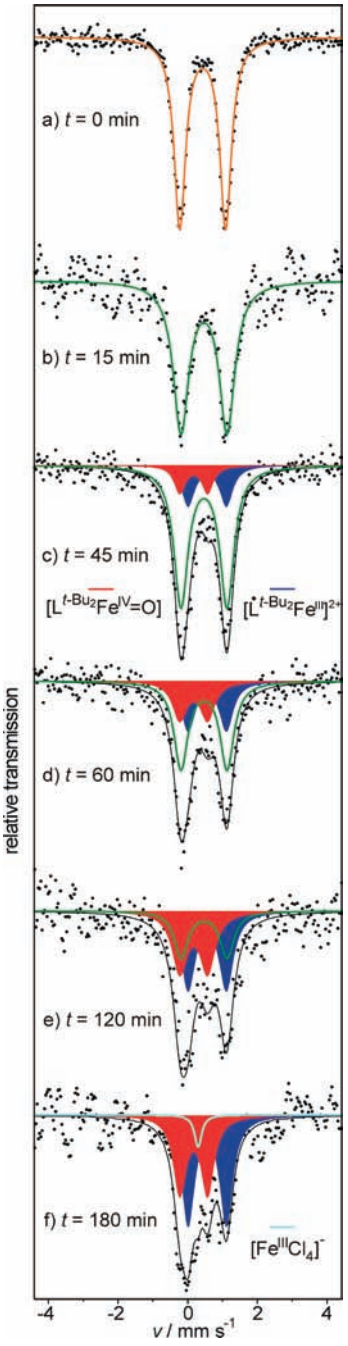

Figure 9. ^{57}Fe Mössbauer spectra recorded at 80 K in CH_2Cl_2 solutions. (a) Spectrum of the starting complex [$L^{t\text{-}Bu_2}$Fe(μ-O)Fe$L^{t\text{-}Bu_2}$]. (b)−(f) Spectra recorded after the oxidation to [$L^{t\text{-}Bu_2}$Fe(μ-O)Fe$L^{t\text{-}Bu_2}$]$^{2+}$ using 2 equiv of **AR** recorded on samples at individual times. Experimental data are given by black dots. The simulations are based on a strategy explained in the text. The sum of all individual spectra is given by the solid thin black line.

Fits to a second order reaction provide less good reproductions of the experimental data. Analysis according to an Eyring plot reveals the activation parameters $\Delta H^{\ddagger} = (51 \pm 1)$ kJ mol^{-1} and $\Delta S^{\ddagger} = -(90 \pm 6)$ J (mol K)$^{-1}$.

3.11.2. [$L^{t\text{-}Bu_2}$Fe(μ-O)Fe$L^{t\text{-}Bu_2}$]$^{2+}$. Solutions of [$L^{t\text{-}Bu_2}$Fe(μ-O)Fe$L^{t\text{-}Bu_2}$]$^{2+}$ were generated by addition of 2 equiv of **AR** to [$L^{t\text{-}Bu_2}$Fe(μ-O)Fe$L^{t\text{-}Bu_2}$] in CH_2Cl_2 at temperatures between −20 °C and −40 °C. Figure 10b shows a representative time-dependence for the decay reaction at −40 °C. There are significant differences to the decay reaction of the

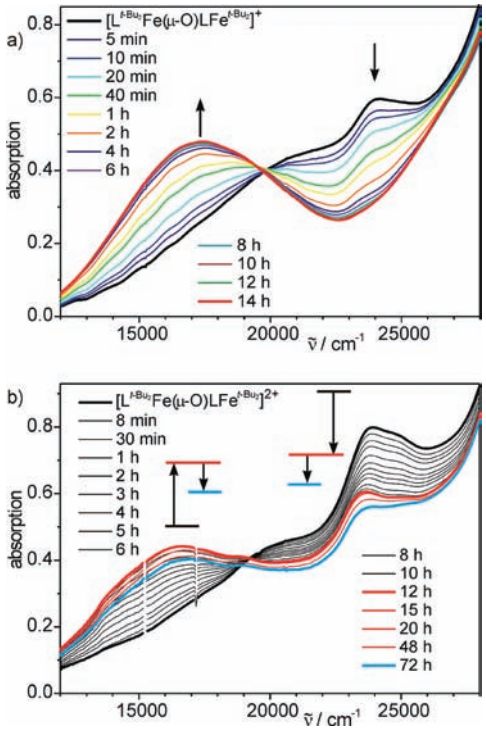

Figure 10. (a) Electronic absorption spectra of the decay of [$L^{t\text{-}Bu_2}$Fe(μ-O)Fe$L^{t\text{-}Bu_2}$]$^{+}$, recorded at −40 °C. (b) Electronic absorption spectra of the decay of [$L^{t\text{-}Bu_2}$Fe(μ-O)Fe$L^{t\text{-}Bu_2}$]$^{2+}$, recorded at −40 °C.

monocation [$L^{t\text{-}Bu_2}$Fe(μ-O)Fe$L^{t\text{-}Bu_2}$]$^{+}$. The most apparent observation is that the decay reaction of the dication is slower than the decay reaction of the monocation. The strong absorption feature at 23900 cm^{-1} with a shoulder at 24800 cm^{-1} decreases slowly over three days. A new strong absorption feature with a maximum at 16700 cm^{-1} appears, which is shifted 800 cm^{-1} to lower energy in comparison to the maximum formed in the decay of the monocation [$L^{t\text{-}Bu_2}$Fe(μ-O)Fe$L^{t\text{-}Bu_2}$]$^{+}$. However, this maximum does not show a continuous increase over 3 days but exhibits its strongest intensity after 12 h, after which it slowly decreases and shifts to 17000 cm^{-1}.

It can be assumed that the decay of the dicationic intermediate [$L^{t\text{-}Bu_2}$Fe(μ-O)Fe$L^{t\text{-}Bu_2}$]$^{2+}$ results in the formation of two new intermediates [$L^{t\text{-}Bu_2}Fe^{IV}$=O] and [$^{\bullet}L^{t\text{-}Bu_2}Fe^{III}$]$^{2+}$ (see Discussion), which should decay with two different rate constants. Because of this complexity, we refrain from a complete kinetic analysis. To obtain some quantitative estimate for the decay of [$L^{t\text{-}Bu_2}$Fe(μ-O)Fe$L^{t\text{-}Bu_2}$]$^{2+}$, we have tried to fit the time-dependence at 16700 cm^{-1}, 23900 cm^{-1}, and 23560 cm^{-1} to a first order reaction using three exponentials to account for all decay reactions. The rate constants obtained at the three wavelengths at a given temperature differ slightly, and mean values have been used. It must be stressed that the accuracy of all values given for the decay reaction of the dication is lower than for the decay reaction of the monocation. However, the trend observed in the spectra (Figure 10b) is also expressed in the values for the rate constants of the decay of [$L^{t\text{-}Bu_2}$Fe(μ-O)Fe$L^{t\text{-}Bu_2}$]$^{2+}$ of $k = 3.8(\pm 0.5) \times 10^{-5}$ s^{-1} at −40 °C. The temperature dependence provides activation parameters of $\Delta H^{\ddagger} = 68(\pm 4)$ kJ mol^{-1} and $\Delta S^{\ddagger} = -36(\pm 10)$ J (mol K)$^{-1}$ as estimates.

To obtain an independent spectroscopic handle for this reaction mechanism proposal, we have followed the

Table 3. Fit Results to the Mössbauer Spectra Recorded during the Decay of $[L^{t\text{-}Bu_2}Fe(\mu\text{-}O)FeL^{t\text{-}Bu_2}]^{2+}$

t	δ/mm s^{-1}	$\lvert\Delta E_Q\rvert$/mm s^{-1}	Γ/mm s^{-1}	% area	assignment
0[a]	0.44	1.32	0.41	100	$[L^{t\text{-}Bu_2}Fe^{III}(\mu\text{-}O)Fe^{III}L^{t\text{-}Bu_2}]$
15 min	0.47	1.32	0.54	100	$[L^{t\text{-}Bu_2}Fe^{III}(\mu\text{-}O)Fe^{III}L^{t\text{-}Bu_2}]^{2+}$
45 min	0.47	1.32	0.49	70	$[L^{t\text{-}Bu_2}Fe^{III}(\mu\text{-}O)Fe^{III}L^{t\text{-}Bu_2}]^{2+}$
	0.17	0.80	0.39	11	$[L^{t\text{-}Bu_2}Fe^{IV}{=}O]$
	0.56	1.10	0.45	19	$[^{\bullet}L^{t\text{-}Bu_2}Fe^{III}]^{2+}$
1 h	0.47	1.32	0.48	50	$[L^{t\text{-}Bu_2}Fe^{III}(\mu\text{-}O)Fe^{III}L^{t\text{-}Bu_2}]^{2+}$
	0.17	0.80	0.50	23	$[L^{t\text{-}Bu_2}Fe^{IV}{=}O]$
	0.56	1.10	0.47	27	$[^{\bullet}L^{t\text{-}Bu_2}Fe^{III}]^{2+}$
2 h	0.47	1.32	0.48	24	$[L^{t\text{-}Bu_2}Fe^{III}(\mu\text{-}O)Fe^{III}L^{t\text{-}Bu_2}]^{2+}$
	0.17	0.80	0.53	34	$[L^{t\text{-}Bu_2}Fe^{IV}{=}O]$
	0.56	1.10	0.49	41	$[^{\bullet}L^{t\text{-}Bu_2}Fe^{III}]^{2+}$
3 h	0.17	0.80	0.45	39	$[L^{t\text{-}Bu_2}Fe^{IV}{=}O]$
	0.56	1.10	0.45	56	$[^{\bullet}L^{t\text{-}Bu_2}Fe^{III}]^{2+}$
	0.30	0	0.28	5	$[Fe^{III}Cl_4]^-$

[a] Measured without addition of oxidant.

decay reaction of $[L^{t\text{-}Bu_2}Fe(\mu\text{-}O)FeL^{t\text{-}Bu_2}]^{2+}$ by time-dependent Mössbauer spectroscopy. A solution of $[L^{t\text{-}Bu_2}Fe(\mu\text{-}O)FeL^{t\text{-}Bu_2}]^{2+}$ was generated by addition of 2 equiv of **AR** to $[L^{t\text{-}Bu_2}Fe(\mu\text{-}O)FeL^{t\text{-}Bu_2}]$ in CH_2Cl_2 at −30 °C and samples were taken after 45, 60, 120, and 180 min (Figure 9c−f). Despite the bad signal-to-noise ratio, there are two trends visible: (*i*) between the two main doublet lines arises some intensity, and (*ii*) the overall intensity of the low velocity line increases in comparison to the high velocity line. Fits and simulations to individual spectra yielded a multitude of possible solutions. However, the requirement of consistency with all physicochemical data presented in this manuscript reduces the amount of possible solutions. The spectrum at t = 15 min corresponds to the dication $[L^{t\text{-}Bu_2}Fe(\mu\text{-}O)FeL^{t\text{-}Bu_2}]^{2+}$ in accordance with the time-dependent UV−vis spectra. As this species decays, the signals of the decay products must appear. According to the electronic absorption spectra, there should be two new subspectra. At the same time, the isomer shift and quadrupole splitting of the starting dication is not allowed to change. Furthermore, the isomer shift and quadrupole splitting of the new subspectra were not allowed to change in the time-course of the reaction. The final product of the decay reaction is $[Fe^{III}Cl_4]^-$ (vide infra). By following these restrictions, a consistent simulation of the time-course of the Mössbauer spectra has been obtained, which accounts for the intensity in between the two central lines and the shift in intensity from the high-velocity line to the low-velocity line (Table 3).

The spectrum recorded after 45 min could be fitted by adding two subspectra to the subspectrum of the starting dication. The subspectrum shown in red in Figure 9c has a low isomer shift of 0.17 mm s^{-1} consistent with the formation of an $Fe^{IV}{=}O$ species. The second subspectrum shown in blue has an isomer shift of 0.56 mm s^{-1}, which is consistent with an Fe^{III} phenoxyl radical species. The higher isomer shift can be explained by the loss of the highly covalent oxo unit and the coordination of the oxidized ligand radical. These two subspectra gain intensity in the time-course, while the subspectrum of the starting dication decreases in intensity. In the spectrum recorded after 3 h, the starting dication is not apparent, which is consistent with the rate constant estimated for the decay at −30 °C. A singlet at 0.30 mm s^{-1} corresponds to the formation of $[Fe^{III}Cl_4]^-$.

Although the signal-to-noise ratio of the Mössbauer spectra is not good enough for meaningful simulations of the individual spectra, a self-consistent global simulation of all spectra with a minimum number of species could be performed. Furthermore, other experimental data presented herein support the simulations. In this respect, it is quite pleasing to note that simulated fraction for $[L^{t\text{-}Bu_2}Fe(\mu\text{-}O)FeL^{t\text{-}Bu_2}]^{2+}$ of 70% at 45 min and 50% at 60 min corresponds quite well with lifetime of ∼45 min at −30 °C obtained from the UV−vis kinetic analysis.

3.12. Product Analysis. To obtain insight into the nature of the final decay products, the decay solutions of $[L^{t\text{-}Bu_2}Fe(\mu\text{-}O)FeL^{t\text{-}Bu_2}]^+$ and $[L^{t\text{-}Bu_2}Fe(\mu\text{-}O)FeL^{t\text{-}Bu_2}]^{2+}$ were warmed to room temperature and kept for 24 h. The decay of $[L^{t\text{-}Bu_2}Fe(\mu\text{-}O)FeL^{t\text{-}Bu_2}]^+$ results in a blue solution **A**, and the decay of $[L^{t\text{-}Bu_2}Fe(\mu\text{-}O)FeL^{t\text{-}Bu_2}]^{2+}$ in a yellow solution **B**. The blue color of **A** arises from an intense band at 17200 cm^{-1}, which almost coincides with the band of $[L^{t\text{-}Bu_2}FeCl]$ at 17500 cm^{-1}.[41] The yellow color of **B** corresponds to a spectrum with the lowest energy band at 27800 cm^{-1}, which indicates a complete decomplexation of the ligand $(L^{t\text{-}Bu_2})^{2-}$.

The Fe K-edges of **A** and **B** are shown together with that of $[L^{t\text{-}Bu_2}Fe(\mu\text{-}O)FeL^{t\text{-}Bu_2}]^+$ and $[L^{t\text{-}Bu_2}Fe(\mu\text{-}O)FeL^{t\text{-}Bu_2}]^{2+}$ in Figure 11. The pre-edge of **A** is only slightly shifted to lower energy, whereas the pre-edge of **B** exhibits an increased intensity (consistent with the presence of a T_d-$[Fe^{III}Cl_4]^-$ product) with no shoulders.

The edges exhibit pronounced shoulders at 7122.0 eV for **A** and 7121.3 eV for **B**. Consistent with the results of EXAFS (see below), these shoulders are attributed to the presence of Fe^{III}−Cl bonds.[63] The EXAFS spectra and the corresponding Fourier transforms are shown in Figure 11b and c, respectively. The higher intensity of the EXAFS signal and in the FT of **A** and even more pronounced in **B** in comparison to the monocation $[L^{t\text{-}Bu_2}Fe(\mu\text{-}O)FeL^{t\text{-}Bu_2}]^+$ and the dication $[L^{t\text{-}Bu_2}Fe(\mu\text{-}O)FeL^{t\text{-}Bu_2}]^{2+}$, indicates a more regular coordination environment with equal iron-ligand vectors. Fitting of **B** provides four Fe−Cl vectors, which corresponds to the presence of $[Fe^{III}Cl_4]^-$ as only Fe species present in **B**. This is corroborated by a Mössbauer spectrum of **B**, which exhibits a single line, which can be fitted with an isomer shift

(63) Kau, L.-S.; Spira-Solomon, D. J.; Penner-Hahn, J. E.; Hodgson, K. O.; Solomon, E. I. *J. Am. Chem. Soc.* **1987**, *109*, 6433–6442.

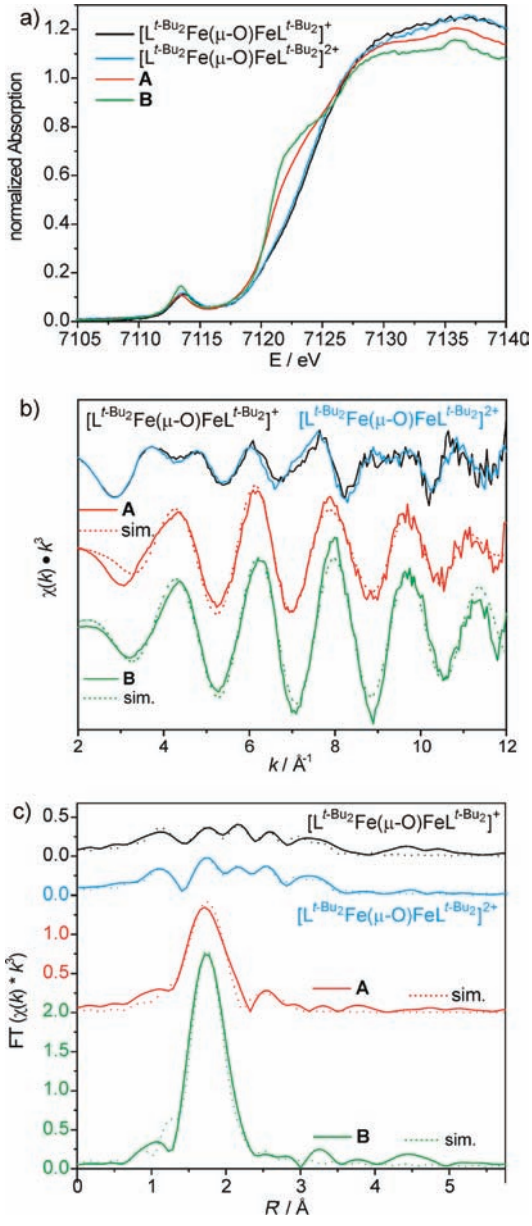

Figure 11. Fe K-edge XAS measurements on the final reaction solution of the mono-oxidized $[L^{t\text{-}Bu_2}Fe(\mu\text{-}O)FeL^{t\text{-}Bu_2}]^{+}$ (**A**) and double-oxidized $[L^{t\text{-}Bu_2}Fe(\mu\text{-}O)FeL^{t\text{-}Bu_2}]^{2+}$ (**B**): (a) normalized K-edges, (b) EXAFS data and their simulations, (c) corresponding non-phase shift corrected Fourier transforms and their simulations.

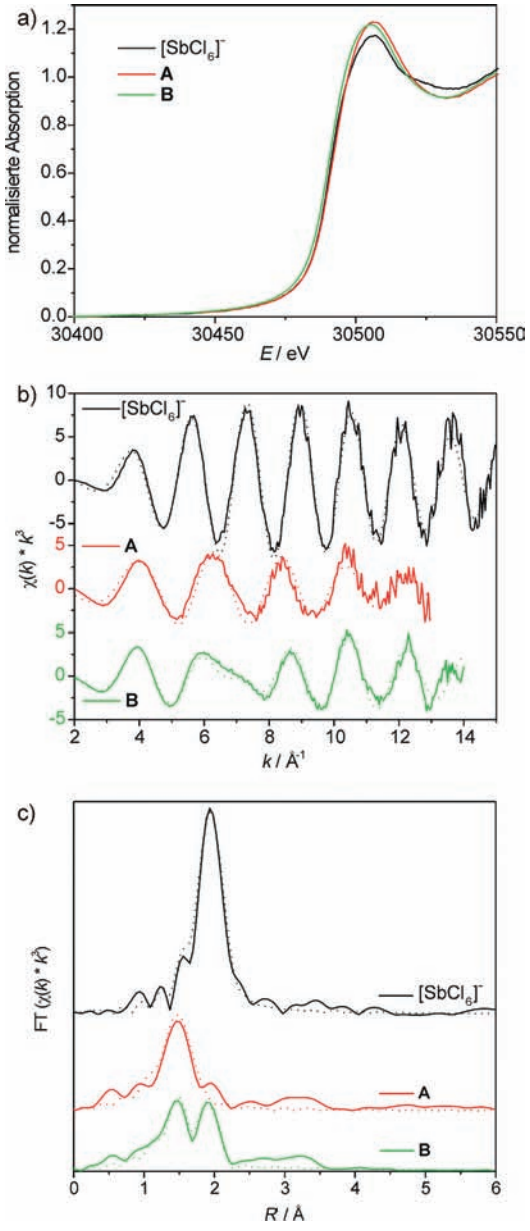

Figure 12. Sb K-edge measurements on the final product solutions of mono-oxidized $[L^{t\text{-}Bu_2}Fe(\mu\text{-}O)FeL^{t\text{-}Bu_2}]^{+}$ (**A**) and double-oxidized $[L^{t\text{-}Bu_2}Fe(\mu\text{-}O)FeL^{t\text{-}Bu_2}]^{2+}$ (**B**) and $[SbCl_6]^{-}$ for comparison: (a) edges, (b) EXAFS data (solid lines) and their simulations (dotted lines), and (c) corresponding non-phase shift corrected Fourier transforms (solid lines) and their simulations (dotted lines).

of 0.30 mm s^{-1} and no quadrupole splitting. Fitting the EXAFS of **A** needed also some Fe−O/N vectors and Fe−C vectors (Supporting Information, Table S9). By considering the typical error of ±1 in the number of donor atoms in EXAFS, these results in combination with the UV−vis data suggest the presence of $[L^{t\text{-}Bu_2}Fe^{III}]^{+}$ and $[Fe^{III}Cl_4]^{-}$ in solution **A**.

The unexpected chloride coordination to iron in the final decay solutions raises the question of the origin of the chloride ions. The reaction solutions exhibit two sources of chlorine, that is, the solvent CH_2Cl_2 and the counterion $[SbCl_6]^{-}$ of the oxidant **AR**. Performing the two-electron oxidation of $[L^{t\text{-}Bu_2}Fe(\mu\text{-}O)FeL^{t\text{-}Bu_2}]$ in CD_2Cl_2 results in no variation in the time-dependence of the electronic absorption spectra in comparison with the reaction under the same conditions in CH_2Cl_2.

In contrast, Sb X-ray absorption spectroscopy gives strong evidence that the chloride ions in **A** and **B** arise from $[SbCl_6]^{-}$. Figure 12 provides the Sb K-edges, the EXAFS, and the corresponding Fourier transforms of **A** and **B** together with that of a solution of $[SbCl_6]^{-}$ for comparison. The high energy of the Sb K-edge results in broad features. However, the EXAFS clearly shows that $[SbCl_6]^{-}$ is not the primary species present in **A** and **B**. Fitting of solutions **A** and **B** required the incorporation of Sb−N/O scatterers in addition to Sb−Cl scatterers (Supporting Information, Table S9). These Sb XAS measurements therefore provide strong evidence that the chloride ions coordinated to Fe in **A** and **B** originate from the **AR** counteranion $[SbCl_6]^{-}$.

4. Discussion

4.1. Influence of the Remote Substituents on Properties Reflecting Differences in the Electronic Structures. The three complexes [$L^{t\text{-}Bu_2}Fe(\mu\text{-}O)FeL^{t\text{-}Bu_2}$], [$L^{Me_2}Fe(\mu\text{-}O)FeL^{Me_2}$], and [$L^{Cl_2}Fe(\mu\text{-}O)FeL^{Cl_2}$] differ only in the remote substituents of the three ligands $H_2L^{t\text{-}Bu_2}$, $H_2L^{Me_2}$, and $H_2L^{Cl_2}$. The Hammett constants σ_p are *t*-Bu −0.20, Me −0.17, and Cl +0.23.[64] These values suggest that the Cl substituent reduces the electron density in the phenolates significantly compared to *t*-Bu and Me. This trend is reflected in the pK_s values of the parent phenols (*t*-Bu 10.4, Me 10.3, and Cl 9.4)[65,66] as well as in the redox potentials for oxidation of the deprotonated phenolates (pH = 12: *t*-Bu 0.30 V, Me 0.31 V, and Cl 0.45 V versus Fc^+/Fc).[67]

The stretching frequency ν(C−O) in the phenols (*t*-Bu 1251 cm^{-1}, Me 1264 cm^{-1}, Cl 1280 cm^{-1}) and in the three ligands ($H_2L^{t\text{-}Bu_2}$ 1234 cm^{-1}, $H_2L^{Me_2}$ 1242 cm^{-1}, $H_2L^{Cl_2}$ 1275 cm^{-1}) provides a different measure of the electron densities in the phenol rings. Because of the reduced electron density in the benzene rings of $H_2L^{Cl_2}$ the phenol oxygen atoms have to compensate this effect by a stronger C═O double bond character, which leads to a higher ν(C−O) stretching frequency. While both electron-donating *t*-Bu and Me groups reduce this double bond character, the *t*-Bu groups have a significantly stronger effect than the Me substituents.

Although spectroscopic methods are generally more sensitive to changes in the electronic structure than bond distances, the higher double bond character of $H_2L^{Cl_2}$ is also visible in the smaller bond length of 1.349(2) Å compared to 1.370(1) Å in $H_2L^{Me_2}$. This trend is also visible in the $C-O^{Ph}$ bond lengths in the three complexes with 1.32 Å for [$L^{Cl_2}Fe(\mu\text{-}O)FeL^{Cl_2}$], 1.34 Å for [$L^{Me_2}Fe(\mu\text{-}O)FeL^{Me_2}$], and 1.35 Å for [$L^{t\text{-}Bu_2}Fe(\mu\text{-}O)FeL^{t\text{-}Bu_2}$].

These changes in the electron densities of the phenolate oxygen atoms should have implications for the electron-donating abilities of the three ligands in the complexes. This is reflected in the differences in the $Fe-O^{Ph}$ bond length, which is short for [$L^{t\text{-}Bu_2}Fe(\mu\text{-}O)FeL^{t\text{-}Bu_2}$] at 1.86 Å and longer for [$L^{Me_2}Fe(\mu\text{-}O)FeL^{Me_2}$] at 1.90 Å and [$L^{Cl_2}Fe(\mu\text{-}O)FeL^{Cl_2}$] at 1.91 Å.

The different charge-donating abilities of the three ligands should consequently influence the electron donation from the bridging oxo ions in accordance to Pauling's electroneutrality principle.[68] The low value of the ν_{as}(Fe−O−Fe) stretching frequency of 810 cm^{-1} for [$L^{t\text{-}Bu_2}Fe(\mu\text{-}O)FeL^{t\text{-}Bu_2}$] in comparison to 817 cm^{-1} for [$L^{Me_2}Fe(\mu\text{-}O)FeL^{Me_2}$] and 829 cm^{-1} for [$L^{Cl_2}Fe(\mu\text{-}O)FeL^{Cl_2}$] reflects differences in the electron-donating properties of the ligands. It is interesting to compare these ν_{as}(Fe−O−Fe) stretching frequencies to a correlation of Sanders-Loehr et al. for oxo-bridged dinuclear ferric complexes and enzymes, which are mainly composed of satured/unsaturated nitrogen donor atoms and carboxylate oxygen donor atoms.[69] For linear Fe−O−Fe units, ν_{as} of ∼870 cm^{-1} were experimentally found, while ν_{as} should be around 855 cm^{-1} at the angle observed for [$L^{Cl_2}Fe(\mu\text{-}O)FeL^{Cl_2}$]. The strongly reduced values for ν_{as} in the three complexes reported herein are a clear indication of the reduced covalency of the $Fe-O^{oxo}$ bond because of the high covalency of the three phenolate ligands irrespective of the remote substituents.

The $Fe^{III}-O-Fe^{III}$ unit in [$L^{t\text{-}Bu_2}Fe(\mu\text{-}O)FeL^{t\text{-}Bu_2}$] and [$L^{Me_2}Fe(\mu\text{-}O)FeL^{Me_2}$] is linear, while it is bent in [$L^{Cl_2}Fe(\mu\text{-}O)FeL^{Cl_2}$] with an angle of 166°. As this bending is observed in two independent crystal structures, packing effects cannot be responsible; it must rather be of electronic origin. The lower electron donating ability of $(L^{Cl_2})^{2-}$ in comparison to $(L^{t\text{-}Bu_2})^{2-}$ and $(L^{Me_2})^{2-}$ might force the Fe−O−Fe unit to bend to optimize the electron donation from the oxo group by σ- and π-bonding interactions.

This effect is also evident in the exchange coupling constant *J*, which is −89 cm^{-1} for [$L^{t\text{-}Bu_2}Fe(\mu\text{-}O)FeL^{t\text{-}Bu_2}$] and −98 to −100 cm^{-1} for [$L^{Me_2}Fe(\mu\text{-}O)FeL^{Me_2}$] and [$L^{Cl_2}Fe(\mu\text{-}O)FeL^{Cl_2}$]. The strength of the exchange coupling constants reflects the strengths of the $Fe^{III}-O^{oxo}$ covalency, which is also reflected in the $Fe-O^{oxo}$ bond distance[70] and to a minor extent in the $Fe-O^{oxo}-Fe$ angle.[56] The strong electron donation of the *t*-Bu ligand results in the lowest $Fe^{III}-O^{oxo}$ covalency and thus the lowest exchange coupling. The close resemblance of the coupling constant for the Me and Cl ligands despite their different electron donating capabilities implies the effects of the bending in [$L^{Cl_2}Fe(\mu\text{-}O)FeL^{Cl_2}$], which influences not only $\pi-\pi$ and $\sigma-\sigma$ pathways but also $\sigma-\pi$ exchange pathways.[71]

The reverse influence, that is, the influence of the strong $Fe-O^{oxo}$ covalency on the $Fe-O^{Ph}$ bonding, is evidenced by electronic absorption spectroscopy. The $p_\pi \rightarrow d_{\pi^*}$ transition in the square-pyramidal mononuclear complex [$L^{t\text{-}Bu_2}FeCl$] appears at 17500 cm^{-1}.[41] Using [$L^{t\text{-}Bu_2}FeCl$] as a reference, the differences between the weakly electron-donating chloride ligand and the strongly electron-donating oxo ligand are visible (the oxo ligand does not reflect a monatomic oxo group but an oxo ligand coordinated to one Fe^{III} complex fragment). The oxo ligand shifts this transition to 23000−25000 cm^{-1} in the dinuclear complexes. The strong electron donation of the oxo group leads to higher electron densities at the ferric ion and an increase in energy of all d orbitals. Therefore, the d orbitals are energetically more separated from the phenolate-based orbitals, resulting in a reduced covalency.

The comparison of the $p_\pi \rightarrow d_{\pi^*}$ transition for the diferric oxo-bridged complexes ([$L^{t\text{-}Bu_2}Fe(\mu\text{-}O)FeL^{t\text{-}Bu_2}$] 23200 cm^{-1}, [$L^{Me_2}Fe(\mu\text{-}O)FeL^{Me_2}$] 24400 cm^{-1}, [$L^{Cl_2}Fe(\mu\text{-}O)FeL^{Cl_2}$] 24600 cm^{-1}) reveals that the *t*-Bu ligand leads to the strongest $Fe-O^{Ph}$ covalency. The exact energies of these transitions are dependent on several parameters, for example, the phenolate σ and π orbital energies, which depend on the phenolate substituent, the strength of the $Fe-O^{Ph}$ bonding, which also depends on

(64) Hansch, C.; Leo, A.; Taft, R. W. *Chem. Rev.* **1991**, *91*, 165–195.
(65) Hanai, T.; Koizumi, K.; Kinoshita, T.; Arora, R.; Ahmed, F. *J. Chromatogr. A* **1997**, *762*, 55–61.
(66) Stradins, J.; Hasanli, B. *Electroanal. Chem.* **1993**, *353*, 57–69.
(67) Li, C.; Hoffman, M. Z. *J. Phys. Chem. B* **1999**, *103*, 6653–6656.
(68) Glaser, T.; Hedman, B.; Hodgson, K. O.; Solomon, E. I. *Acc. Chem. Res.* **2000**, *33*, 859–868.
(69) Sanders-Loehr, J.; Wheeler, W. D.; Shiemke, A. K.; Averill, B. A.; Loehr, T. M. *J. Am .Chem. Soc.* **1989**, *111*, 8084–8093.
(70) Gorun, S. M.; Lippard, S. J. *Inorg. Chem.* **1991**, *30*, 1625–1630.
(71) Hotzelmann, R.; Wieghardt, K.; Florke, U.; Haupt, H. J.; Weatherburn, D. C.; Bonvoisin, J.; Blondin, G.; Girerd, J. J. *J. Am. Chem. Soc.* **1992**, *114*, 1681–1696.

the orbital energies, and on the Fe−O^{oxo} bonding interaction. However, the higher electron density in the phenolates for X = *t*-Bu and therefore the higher phenolate orbital energies should have the main contribution to the low energy shift.

In summary, the change of the remote substituents in the diferric oxo-bridged complexes has significant influence on the overall electronic structure of the central Fe−O^{Ph} and, thus, Fe−O^{oxo} core. While all spectroscopic, structural, and magnetic parameters demonstrate that the *t*-Bu ligand has the strongest and the Cl ligand has the lowest electron-donating ability, the properties of [L^{Me_2}Fe(μ-O)FeL^{Me_2}] are not directly correlated to the Hammett constant σ_p. This implies that the electronic structure has significant contributions from π-bonding interactions, which has already been shown for the mononuclear complexes,[41] and that the π-bonding is flexible to compensate variations in electron donation.

4.2. Influence of the Remote Substituents on Redox Potentials and Stabilities of the Oxidized Species. The differences in the electronic structures in the three complexes discussed above have significant impact in the redox properties of the three complexes (all potentials are referenced to Fc^+/Fc). The three complexes are irreversibly reduced at −1.30 V ([L^{Cl_2}Fe(μ-O)FeL^{Cl_2}]), −1.75 V ([L^{Me_2}Fe(μ-O)FeL^{Me_2}]), and −2.05 V ([$L^{t\text{-}Bu_2}$Fe(μ-O)Fe$L^{t\text{-}Bu_2}$]). These reductions can be assigned to the reduction of the dinuclear complexes to the dinuclear monoanions. The non-reversibility may either be attributed to a break of an Fe^{II}−O^{oxo} bond and cleavage into two mononuclear subunits or to a protonation of the oxo-bridge in the reduced $Fe^{II}Fe^{III}$ form. The huge potential differences tremendously reflect the changes in the electron-donating abilities of the ligand. The low electron-donating ability of the Cl ligand results in a low electron density at the Fe^{III} site making it easiest to reduce. The higher electron-donating properties of the Me and *t*-Bu groups leads to strong cathodical shifts, where again the Me and *t*-Bu substituents lead to pronounced differences, which are not expected solely according to the Hammett constants.

Again, the comparison with the mononuclear complex [$L^{t\text{-}Bu_2}$FeCl], which shows an irreversible reduction at −1.10 V is an impressive experimental demonstration of the strong electron-donating properties of the oxo ligand in comparison with the Cl ligand.[41] The ligand-centered oxidation in [$L^{t\text{-}Bu_2}$FeCl] at +0.55 V is facilitated to +0.27 V in [$L^{t\text{-}Bu_2}$Fe(μ-O)Fe$L^{t\text{-}Bu_2}$]. The strong electron-donation of the oxo ligand leads to a lower covalency of the Fe^{III}−O^{Ph} bond, a higher electron density in the phenolate, and thus an easier oxidation evidenced by the lower potential.

The three diferric complexes can be oxidized at relatively moderate potentials. However, only [$L^{t\text{-}Bu_2}$Fe(μ-O)Fe$L^{t\text{-}Bu_2}$] exhibits two reversible oxidations at commonly used scan rates. Only the use of high scan rates allows the observation of a reductive peak for [L^{Me_2}Fe(μ-O)FeL^{Me_2}] and [L^{Cl_2}Fe(μ-O)FeL^{Cl_2}]. In contrast to the potentials for reduction, the potentials for oxidation are relatively close for [$L^{t\text{-}Bu_2}$Fe(μ-O)Fe$L^{t\text{-}Bu_2}$] at 0.27 V and [L^{Me_2}Fe(μ-O)FeL^{Me_2}] at 0.29 V, whereas [L^{Cl_2}Fe(μ-O)FeL^{Cl_2}] is much more difficult to oxidize at 0.87 V because of the low electron-donating ability of the Cl substituent.

4.3. Electronic Structure of [$L^{t\text{-}Bu_2}$Fe(μ-O)Fe$L^{t\text{-}Bu_2}$]$^+$ and [$L^{t\text{-}Bu_2}$Fe(μ-O)Fe$L^{t\text{-}Bu_2}$]$^{2+}$. The lifetime of [$L^{t\text{-}Bu_2}$Fe(μ-O)Fe$L^{t\text{-}Bu_2}$]$^+$ and [$L^{t\text{-}Bu_2}$Fe(μ-O)Fe$L^{t\text{-}Bu_2}$]$^{2+}$ allows for the spectroscopic characterization of these intermediates. UV−vis spectro-electrochemistry reveals the appearance of a characteristic band at 24100 cm^{-1} for the monocation and the dication. An analogous strong absorption has been observed in the mono-oxidized [$L^{t\text{-}Bu_2}$FeCl]$^+$ and the dioxidized [$L^{t\text{-}Bu_2}$FeCl]$^{2+}$.[41] An absorption band around ∼24000−25000 cm^{-1} is characteristic for phenoxyl radicals.[39,40,72] Thus, electronic absorption spectroscopy reveals a ligand-centered and not an iron-centered oxidation, leading to a monophenoxyl radical and a diphenoxyl radical complex. This is corroborated by the Mössbauer spectrum of [$L^{t\text{-}Bu_2}$Fe(μ-O)Fe$L^{t\text{-}Bu_2}$]$^{2+}$, which displays no significant changes to the neutral starting complex consistent with the oxidation state Fe^{III} in the dication.

The isotropic EPR spectrum of [$L^{t\text{-}Bu_2}$Fe(μ-O)Fe$L^{t\text{-}Bu_2}$]$^+$ with a very small *g*-shift is consistent with the description of an Fe^{III} h.s.−Fe^{III} h.s.-phenoxyl radical spin system. This $S_1 = S_2 = 5/2$ and $S_3 = 1/2$ system is expected to couple to a spin groundstate $S_t = 1/2$ by antiferromagnetic coupling between the two Fe^{III} ions through the oxo bridge and by the direct overlap of the phenoxyl radical p_π orbital with the Fe^{III} d orbitals. As all three local spins are expected to be isotropic, the spin ground should also be isotropic.

Fe K-edge X-ray absorption spectroscopy of [$L^{t\text{-}Bu_2}$Fe(μ-O)Fe$L^{t\text{-}Bu_2}$]$^+$ and [$L^{t\text{-}Bu_2}$Fe(μ-O)Fe$L^{t\text{-}Bu_2}$]$^{2+}$ also indicates no changes compared to the neutral complex, which would be expected for a metal-centered oxidation to Fe^{IV}. Thus, the spectroscopic characterization of [$L^{t\text{-}Bu_2}$Fe(μ-O)Fe$L^{t\text{-}Bu_2}$]$^+$ and [$L^{t\text{-}Bu_2}$Fe(μ-O)Fe$L^{t\text{-}Bu_2}$]$^{2+}$ unambiguously demonstrates a ligand-centered oxidation to a monophenoxyl radical complex and a diphenoxyl radical complex, respectively, and not to a metal-centered oxidation leading to Fe^{IV} species.

4.4. Mechanism of the Decay of [$L^{t\text{-}Bu_2}$Fe(μ-O)Fe$L^{t\text{-}Bu_2}$]$^+$ and [$L^{t\text{-}Bu_2}$Fe(μ-O)Fe$L^{t\text{-}Bu_2}$]$^{2+}$. The oxidized monocation [$L^{t\text{-}Bu_2}$Fe(μ-O)Fe$L^{t\text{-}Bu_2}$]$^+$ decays with $\tau_{1/2} \approx 27$ min at −40 °C (Scheme 2). The new band at 17500 cm^{-1} indicates the generation of a mononuclear Fe^{III} complex of the ligand $(L^{t\text{-}Bu_2})^{2-}$,[41] which implies a cleavage of an Fe−O^{oxo} bond. The oxidation of [$L^{t\text{-}Bu_2}$Fe(μ-O)Fe$L^{t\text{-}Bu_2}$] at one ligand leads to one electron-deficient half. Considering the charge-donation flexibility of the system (vide supra), the oxo ligand will counter-balance this deficiency by more charge donation to the oxidized half. This leads to an asymmetrical bridging mode of the oxo ligand with a higher covalency and therefore a stronger Fe^{III}−O^{oxo} bond to the oxidized half. Thus, the oxo ligand remains at the oxidized half upon the heterolytic cleavage of the dinuclear unit. The observation of the two fragments [$L^{t\text{-}Bu_2}$Fe]$^+$ and [$L^{t\text{-}Bu_2}$Fe=O]$^+$ in the mass spectra of the neutral complex corroborates the Fe−O^{oxo} bond cleavage. The non-oxidized fragment [$L^{t\text{-}Bu_2}Fe^{III}$]$^+$ appears to be stable and is responsible for the blue color of the final product solution **A**. The second fragment originating from the oxidized half is formally [$^{\bullet}L^{t\text{-}Bu_2}Fe^{III}O$]. However, the decay reaction is characterized by the disappearance of the phenoxyl radical band at 24100 cm^{-1}, which clearly establishes that the oxidation equivalent is no longer localized on

(72) Muller, J.; Weyhermuller, T.; Bill, E.; Hildebrandt, P.; Ould-Moussa, L.; Glaser, T.; Wieghardt, K. *Angew. Chem., Int. Ed.* **1998**, *37*, 616–619.

Scheme 2

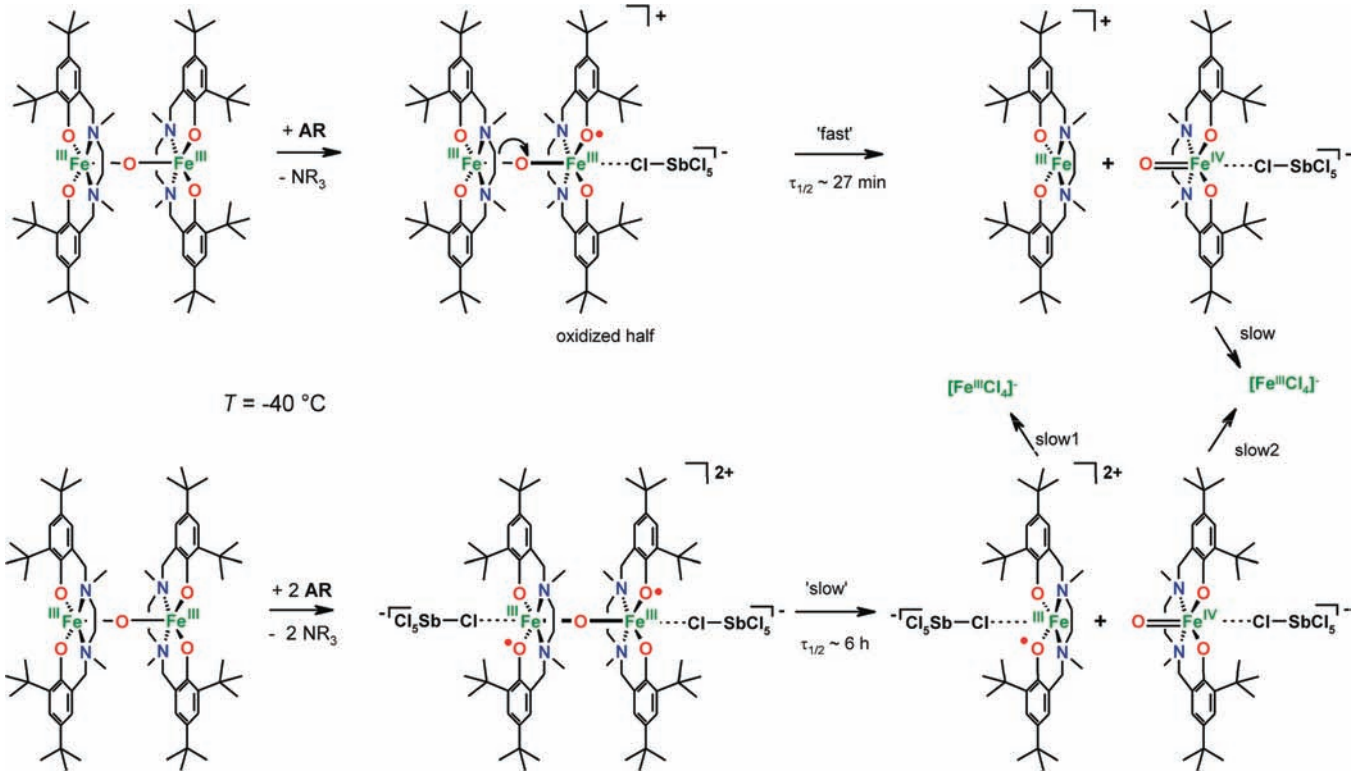

the ligand. We assume that this species relaxes instantaneously by fast intramolecular electron transfer to the ferryl species $[L^{t\text{-}Bu_2}Fe^{IV}{=}O]$, as an Fe^{III}-oxo unit is inherently unstable and the $Fe^{IV}{=}O$ is known to exhibit at least some stability.[73] From final product analysis, it appears that this $Fe^{IV}{=}O$ converts to $[FeCl_4]^-$. The Sb XAS analysis strongly suggests that the Cl^- ions originate from the **AR** counteranion $[SbCl_6]^-$.

$[L^{t\text{-}Bu_2}Fe(\mu\text{-}O)FeL^{t\text{-}Bu_2}]^{2+}$ decays at −40 °C with $\tau_{1/2} \approx$ 6 h (Scheme 2). The strong increase of the band at 16700 cm^{-1} is again consistent with the formation of a mononuclear Fe^{III} complex of the ligand $(L^{t\text{-}Bu_2})^{2-}$ and therefore of a cleavage of an $Fe^{III}{-}O^{oxo}$ bond. Interestingly, the double-oxidized intermediate with a higher reactivity for electron-transfer exhibits a higher stability for $Fe{-}O^{oxo}$ bond breaking than $[L^{t\text{-}Bu_2}Fe(\mu\text{-}O)FeL^{t\text{-}Bu_2}]^+$. As both halves are oxidized in $[L^{t\text{-}Bu_2}Fe(\mu\text{-}O)FeL^{t\text{-}Bu_2}]^{2+}$ and thus electron-deficient, the bridging oxo group has to donate more charge to both halves, resulting in a symmetrical strengthening of both $Fe^{III}{-}O^{oxo}$ bonds. This stronger $Fe^{III}{-}O^{oxo}$ is reflected by $\Delta H^{\ddagger}$ for the decay of the dicationic intermediate of 68 kJ mol^{-1} in contrast to only 51 kJ mol^{-1} for the decay of the mono-oxidized intermediate.

The cleavage of the $Fe^{III}{-}O^{oxo}$ bond yields again formally $[^{\bullet}L^{t\text{-}Bu_2}Fe^{III}O]$, which relaxes to $[L^{t\text{-}Bu_2}Fe^{IV}{=}O]$, and a radical intermediate $[^{\bullet}L^{t\text{-}Bu_2}Fe^{III}]^{2+}$ (Scheme 2). The formulation of the second fragment as a Fe^{III} phenoxyl radical species is consistent with the radical signature at 23700 cm^{-1}, which is still present when the absorption feature at 16700 cm^{-1} is at its turning point in intensity. The changes of the Mössbauer spectra during the decay of $[L^{t\text{-}Bu_2}Fe(\mu\text{-}O)FeL^{t\text{-}Bu_2}]^{2+}$ are also consistent with a decay by the formation of the two intermediates $[L^{t\text{-}Bu_2}Fe^{IV}{=}O]$ and $[^{\bullet}L^{t\text{-}Bu_2}Fe^{III}]^{2+}$. Both of these intermediates finally convert to $[Fe^{III}Cl_4]^-$, which is the only Fe-based species in the final product solution **B**.

Several experimental findings imply that the monocation $[L^{t\text{-}Bu_2}Fe(\mu\text{-}O)FeL^{t\text{-}Bu_2}]^+$ and the dication $[L^{t\text{-}Bu_2}Fe(\mu\text{-}O)FeL^{t\text{-}Bu_2}]^{2+}$ form at least contact pairs with the counteranion $[SbCl_6]^-$. This interpretation is corroborated by the relatively high negative value of the activation entropy $\Delta S^{\ddagger}$, which implies some order in the transition state. Thus, the decay of $[L^{t\text{-}Bu_2}Fe(\mu\text{-}O)FeL^{t\text{-}Bu_2}]^+$ and $[L^{t\text{-}Bu_2}Fe(\mu\text{-}O)FeL^{t\text{-}Bu_2}]^{2+}$ seems to be anion-assisted (Scheme 2). In this respect, it seems feasible that the oxidized mononuclear intermediates, $[L^{t\text{-}Bu_2}Fe^{IV}{=}O]$ and $[^{\bullet}L^{t\text{-}Bu_2}Fe^{III}]^{2+}$, also form contact pairs with $[SbCl_6]^-$, which initiates their decay reaction to $[FeCl_4]^-$.

The ferryl species $[L^{t\text{-}Bu_2}Fe^{IV}{=}O]$ formed by the decay of the oxidized dinuclear complexes is an intermediate. More detailed spectroscopic characterization is prohibited by the presence of several other iron species. Thus, we cannot provide a definitive assignment of its spin state. We can only speculate as the high reactivity of this ferryl species is somewhat counterintuitive to the strongly electron-donating ligand set of $(L^{t\text{-}Bu_2})^{2-}$, which should lead to a stabilization of the $Fe^{IV}{=}O$ unit. Most of the characterized $Fe^{IV}{=}O$ units exhibit a low-spin $Fe^{IV}(S = 1)$ ion[73] and only very few examples of high-spin $Fe^{IV}(S = 2)$ complexes are known.[74−76] The known low-spin $Fe^{IV}(S = 1)$ complexes

(73) Que, L. *Acc. Chem. Res.* **2007**, *40*, 493–500.

(74) Pestovsky, O.; Stoian, S.; Bominaar, E. L.; Shan, X. P.; Munck, E.; Que, L.; Bakac, A. *Angew. Chem., Int. Ed.* **2005**, *44*, 6871–6874.

(75) Anastasi, A. E.; Comba, P.; McGrady, J.; Lienke, A.; Rohwer, H. *Inorg. Chem.* **2007**, *46*, 6420–6426.

(76) England, J.; Martinho, M.; Farquhar, E. R. *Angew. Chem., Int. Ed.* **2009**, *48*, 3622–3626.

are mainly composed of saturated and unsaturated nitrogen donor atoms. The phenolate donors of $(L^{t\text{-}Bu_2})^{2-}$ are strong σ- and also strong π-donor ligands, which decreases the strength of the ligand field. Thus, the high reactivity of $[L^{t\text{-}Bu_2}Fe^{IV}{=}O]$ may be related to a high-spin configuration of the Fe^{IV}($S = 2$) ion, which is generally assumed to be more reactive.[77]

5. Conclusions

(1) Reducing the charge-donating ability of the ligand (i.e., on going from $(L^{t\text{-}Bu_2})^{2-}$ to $(H_2L^{Me_2})^{2-}$ and $(H_2L^{Cl_2})^{2-}$) does not provide access to bis-μ-hydroxo-bridged Fe^{III} complexes, as is observed for the derivatives of the ligand H_2L^H. Even the electron donation of $(L^{Cl_2})^{2-}$ is strong enough to stabilize the five-coordinate complex.

(2) The $Fe^{III}{-}O^{oxo}$ bonds as well as the $Fe^{III}{-}O^{Ph}$ bonds are highly covalent. Variations in the remote ligands lead to compensating effects by the bridging oxo ligand.

(3) The complexes $[L^{t\text{-}Bu_2}Fe(\mu\text{-}O)FeL^{t\text{-}Bu_2}]$, $[L^{Me_2}Fe(\mu\text{-}O)FeL^{Me_2}]$, and $[L^{Cl_2}Fe(\mu\text{-}O)FeL^{Cl_2}]$ exhibit relatively moderate potentials for the oxidation. $[L^{t\text{-}Bu_2}Fe(\mu\text{-}O)FeL^{t\text{-}Bu_2}]$ can be ligand-centered oxidized to form the monophenoxyl radical complex $[^{\bullet}L^{t\text{-}Bu_2}Fe^{III}(\mu\text{-}O)Fe^{III}L^{t\text{-}Bu_2}]^+$ and the diphenoxyl radical complex $[^{\bullet}L^{t\text{-}Bu_2}Fe^{III}(\mu\text{-}O)Fe^{III\bullet}\text{-}L^{t\text{-}Bu_2}]^{2+}$. On the other hand, the oxidized species $[L^{Me_2}Fe(\mu\text{-}O)FeL^{Me_2}]^+$ and $[L^{Cl_2}Fe(\mu\text{-}O)FeL^{Cl_2}]^+$ exhibit stabilities of less than one second.

(4) Even the relatively stable $[L^{t\text{-}Bu_2}Fe(\mu\text{-}O)FeL^{t\text{-}Bu_2}]^+$ and $[L^{t\text{-}Bu_2}Fe(\mu\text{-}O)FeL^{t\text{-}Bu_2}]^{2+}$ compounds undergo decay reactions into mononuclear fragments.

We have used these findings to develop an improved ligand system, which prevents the decay of the oxidized species into mononuclear fragments. The development of this ligand system of the second generation[78] and its application for the synthesis of various dinuclear metal complexes will be published in several forthcoming papers.

Acknowledgment. This work was supported by the Fonds der Chemischen Industrie, the Max-Planck Society, and the DFG. S.D. thanks Cornell University for generous financial support. SSRL operations are funded by the Department of Energy, Office of Basic Energy Sciences. The structural molecular biology program is supported by the National Institute of Health, National Center for Research, Resources, Biomedical Technology Program and by the Department of Energy, Office of Biological and Environmental Research.

Supporting Information Available: Thermal ellipsoid plots of the ligands and the complexes. EXAFS spectra of $[L^{t\text{-}Bu_2}Fe(\mu\text{-}O)FeL^{t\text{-}Bu_2}]$. Magnetic and EPR data. Kinetic analysis of the decay of $[L^{t\text{-}Bu_2}Fe(\mu\text{-}O)FeL^{t\text{-}Bu_2}]^+$. Tables of crystallographic and EXAFS analysis. This material is available free of charge via the Internet at http://pubs.acs.org.

(77) Hirao, H.; Kumar, D.; Que, L., Jr.; Shaik, S. *J. Am .Chem. Soc.* **2006**, *128*, 8590–9606.

(78) Strautmann, J. B. H.; Walleck, S.; Bögge, H.; Stammler, A.; Glaser, T. *Chem. Commun.* **2011**, DOI: 10.1039/C0CC03098H.